



저작자표시-비영리-변경금지 2.0 대한민국

이용자는 아래의 조건을 따르는 경우에 한하여 자유롭게

- 이 저작물을 복제, 배포, 전송, 전시, 공연 및 방송할 수 있습니다.

다음과 같은 조건을 따라야 합니다:



저작자표시. 귀하는 원저작자를 표시하여야 합니다.



비영리. 귀하는 이 저작물을 영리 목적으로 이용할 수 없습니다.



변경금지. 귀하는 이 저작물을 개작, 변형 또는 가공할 수 없습니다.

- 귀하는, 이 저작물의 재이용이나 배포의 경우, 이 저작물에 적용된 이용허락조건을 명확하게 나타내어야 합니다.
- 저작권자로부터 별도의 허가를 받으면 이러한 조건들은 적용되지 않습니다.

저작권법에 따른 이용자의 권리는 위의 내용에 의하여 영향을 받지 않습니다.

이것은 [이용허락규약\(Legal Code\)](#)을 이해하기 쉽게 요약한 것입니다.

[Disclaimer](#)

이학박사학위논문

Molecular Dynamics Simulation Study of
Electric Double Layer Capacitors

분자동역학 전산모사를 통한 전기이중층 축전기의 연구

2018년 8월

서울대학교 대학원
화학부 물리화학 전공
조 성 식

Molecular Dynamics Simulation Study of Electric Double Layer Capacitors

분자동역학 전산모사를 통한 전기이중층 축전기의 연구

지도교수 정 연 준

이 논문을 이학박사 학위논문으로 제출함
2018년 6월

서울대학교 대학원
화학부 물리화학 전공
조 성 식

조성식의 이학박사 학위논문을 인준함
2018년 6월

위원장	<u>석 차 옥</u>	(인)
부위원장	<u>정 연 준</u>	(인)
위원	<u>이 상 엽</u>	(인)
위원	<u>신 석 민</u>	(인)
위원	<u>성 봉 준</u>	(인)

Molecular Dynamics Simulation Study of Electric Double Layer Capacitors

by

Sungsik Jo

Supervised by

Professor **YounJoon Jung**

A Dissertation

Submitted to the Faculty of

Seoul National University

in Partial Fulfillment of

the Requirements for the Degree of

Doctor of Philosophy

August 2018

Department of Chemistry

Graduate School

Seoul National University

Abstract

Electric double layer capacitors (EDLCs) have drawn considerable attention as energy storage devices due to their high capacitance. The differential capacitance (DC) of EDLCs is a function of electric potential because the structure of electric double layer(EDL) is changed. In this thesis, dependence of DC behavior on chemical structure of electrolyte is investigated via molecular dynamics simulation.

In the first part, we investigate how the alkyl chain length of the cation affects their interfacial structure and electrical properties for electric double layer capacitors. As an electrolyte, we consider three different room-temperature ionic liquids (RTILs), each of which is made up of the same anion BF_4^- , and different cations, 1- C_n ($n=2,4,6$)-3-methylimidazolium, respectively. As a whole, cations and anions make layering structures between two parallel electrodes. Cations in the nearest layer orient predominantly in parallel to the electrode. Imidazolium rings of cations form π -stacking with graphene, then the alkyl chains of cations align parallel to the electrode. Differential capacitances in three RTILs are found to decrease with an increase of the magnitude of electrode potentials. The ion size and orientation affect both structure and capacitance behavior. The parallel orientations of

cations become stronger with an increase of the alkyl chain length for the considered RTILs. The differential capacitance tends to decrease with raising the alkyl chain length over a wide range of the electrode potential. This is ascribed to a steric effect caused by larger cation size. It is also found that anodic capacitance is higher than cathodic one due to a higher screening efficiency by small anions, and an asymmetry in the peak of capacitance biased to the cathodic side becomes weaker as the alkyl chain length increases. Comparing electrode charge with ion numbers near the electrodes, with respect to their changes in response to the electrode potential, we find that the interfacial layer of the electrolyte mainly governs capacitive behavior of our systems.

In the second part, charged functional group is systematically attached to anion. Four different ionic liquids are considered as an electrolyte, each of which is combination of the same cation 1-ethyl-3-methylimidazolium ($[\text{emim}]^+$), and different, cyano-containing anions, thiocyanate ($[\text{SCN}]^-$), dicyanamide ($[\text{N}(\text{CN})_2]^-$), tricyanomethanide ($[\text{C}(\text{CN})_3]^-$), and tetracyanoborate ($[\text{B}(\text{CN})_4]^-$), respectively. In particular we investigate how electric double layer structure and electrical properties are affected by the structure of cyano containing anions. Cations and anions make alternating structure near charged electrode. Differential capacitances in four ionic liquids are found to have a maximum value at negative potential. The maximum capacitances are comparable to each other, but the corresponding potential shifts to the negative side as more cyano groups are attached to the anion. Starting from the interfacial layer, the effects of the further ionic layers on differential capacitance are systematically investigated. Comparing charges of the electrode and those of ionic layers, we find that differential capacitance behavior mainly stems

from the ion exchange between electric double layer and bulk region. The ion exchange behaviors are decomposed into cation and anion contributions. The differential charging mechanisms of the system are strongly dependent on the electric potential. The maximum capacitances are consequence of rapid desorption of respective anions.

Keywords: electric double layer capacitor, room-temperature ionic liquid, graphene electrode, alkylimidazolium, differential capacitance, interfacial structure, electric double layer structure, charging mechanism, molecular dynamics simulation

Student Number: 2010-20294

Contents

Abstract	i
1 Overview	1
1.1 Capacitors	1
1.2 Electric double layer capacitors	3
1.3 Shape of DC curves	5
1.4 Ionic liquids	6
I Effects of Alkyl Chain Length in Cation on Interfacial Structure and Differential Capacitance	7
2 Introduction	9
3 Models and Methods	13
4 Results and Discussion	17
4.1 Interfacial Structure	17
4.2 Electric Potentials and Differential Capacitances	25
4.3 Ion Accumulation in the Interfacial Layer	31

5	Conclusions	37
II	Effects of Cyano-Group in Anion on Differential Capacitance and Charging Mechanism	39
6	Introduction	41
7	Models and Methods	47
8	Results and Discussion	51
8.1	Interfacial Structure	51
8.2	Electric Potentials and Differential Capacitances	52
8.3	Ion Exchange in the Electric Double Layer	58
8.4	Differential Charging Mechanism	62
9	Conclusions	69
10	Effects of Alkyl Chain Length in Cation on Charging Mechanism	71
10.1	Ion Exchange in the Electric Double Layer	71
10.2	Differential Charging Mechanism	72
	Appendix	79
A	Ion Number Difference and its Derivative	79
B	Transition from specific ionic layers to electric double layers	81

Bibliography	83
국문초록	99
감사의 글	101

List of Figures

- 1.1 Schematic representation of a capacitor with dielectric material. Red: positive charge, Blue: negative charge, Green: electric field line, Orange: dielectric material. 2
- 1.2 Schematic representation of an electric double layer capacitor. Counterions are accumulated near charged electrodes. Red: positive charge, Blue: negative charge. 4
- 3.1 Snapshot of one of our systems. Yellow: anode with charge $Q_e = +8e$, Blue: cathode with the opposite charge, Red: $[\text{emim}]^+$ cation, Green: BF_4^- anions. Ions in the interfacial layers are highlighted. We can see that a charged electrode attracts counterions and expels coions. 14

- 4.1 Number density distribution functions $n_\alpha(z)$ of cations and anions in three RTILs; (a) [emim]⁺BF₄⁻; (b) [bmim]⁺BF₄⁻; (c) [hmim]⁺BF₄⁻. The cation and anion number density distributions are represented by red and green curves, respectively. The locations of the electrode are indicated by yellow blue (anode) and blue (cathode) vertical lines. Counterions are abundant in the first layer of a charged electrode. Plots are shifted up as total electrode charge Q_e increases from the bottom to the top panel. 18
- 4.2 Schematic representation of the chain angle θ_c and the dihedral angle θ_d in [bmim]⁺. Yellow: graphene electrode, Black: surface normal vector, Red: chain vector, Green: chain angle θ_c , Blue: dihedral angle θ_d 20
- 4.3 Angle probability distributions $P(\theta_c)$ between the surface normal vector and alkyl chain vector of the cation, obtained in (a) [emim]⁺BF₄⁻, (b) [bmim]⁺BF₄⁻ and (c) [hmim]⁺BF₄⁻ at 350K. The chain vector is defined as one from the carbon connected to the imidazolium ring to the terminal one and their normalization satisfies $\int_0^\pi P(\theta_c)\sin\theta_c d\theta_c = 1$ 22
- 4.4 Probability distributions $P(\theta_d)$ of the dihedral angle in the alkyl chain connected to the nitrogen of the imidazolium ring in (a) [bmim]⁺BF₄⁻ and (b) [hmim]⁺BF₄⁻ at 350K. Results for cathode and anode were obtained with $Q_e = \pm 2e$. $P(\theta_d)$ is normalized by $\int_0^{2\pi} P(\theta_d)d\theta_d = 1$ 23

4.5	Snapshots of alkyimidazolium cations in the first solvent layer from the neutral electrodes, obtained in (a) [emim] ⁺ BF ₄ ⁻ , (b) [bmim] ⁺ BF ₄ ⁻ , and (c) [hmim] ⁺ BF ₄ ⁻ at 350 K.	24
4.6	Charge density distribution functions $\rho_\alpha(z)$ in three RTILs; (a) [emim] ⁺ BF ₄ ⁻ ; (b) [bmim] ⁺ BF ₄ ⁻ ; (c) [hmim] ⁺ BF ₄ ⁻ . The cation, anion and total charge density distributions are represented by red, green, and purple curves, respectively. Plots are shifted up as total electrode charge Q_e increases from the bottom to the top panel.	26
4.7	Electric potential $\Phi_{\text{total}}(z)$ in three RTILs; top: [emim] ⁺ BF ₄ ⁻ ; middle: [bmim] ⁺ BF ₄ ⁻ ; bottom: [hmim] ⁺ BF ₄ ⁻ . Yellow: anode, Blue: cathode.	28
4.8	Differential capacitances c and electrode charge Q_e as a function of $\Delta\Phi_{\text{half}}$, obtained in [emim] ⁺ BF ₄ ⁻ , [bmim] ⁺ BF ₄ ⁻ and [hmim] ⁺ BF ₄ ⁻ at 350K.	30
4.9	Electrode charge Q_e and ion number difference ΔN in three RTILs; (a) [emim] ⁺ BF ₄ ⁻ ; (b) [bmim] ⁺ BF ₄ ⁻ ; (c) [hmim] ⁺ BF ₄ ⁻ . ΔN has two values at $\Delta\Phi_{\text{half}} = 0$	32
4.10	(a) Differential ion capacity R as a function of $\Delta\Phi_{\text{half}}$, obtained in three RTILs. Differential capacitance c and differential ion capacity R are compared for each system; (b) [emim] ⁺ BF ₄ ⁻ ; (c) [bmim] ⁺ BF ₄ ⁻ ; (d) [hmim] ⁺ BF ₄ ⁻	34

- 7.1 Representative snapshot of our systems. Blue: cathode with charge $Q_e = -32e$, Yellow: anode with the opposite charge, Red: $[\text{emim}]^+$ cations, Green: $[\text{N}(\text{CN})_2]^-$ anions, Highlighted: Ions in the interfacial layers. Counterions are attracted to and coions are expelled from the charged electrodes. 49
- 8.1 Number density distribution $n_\alpha(z)$ of the ions in four ionic liquids: (a) $[\text{emim}]^+[\text{SCN}]^-$, (b) $[\text{emim}]^+[\text{N}(\text{CN})_2]^-$, (c) $[\text{emim}]^+[\text{C}(\text{CN})_3]^-$, and (d) $[\text{emim}]^+[\text{B}(\text{CN})_4]^-$. The cation and anion number density distributions are represented by red and green curves, respectively. The locations of the electrode are indicated by yellow blue (anode) and blue (cathode) vertical lines. Black vertical lines are the borderlines between ionic layers. Counterions are abundant in the interfacial layer. Plots in the upper panels are the cases with the largest electrode charge Q_e 53
- 8.2 Charge density distribution $\rho_\alpha(z)$ of the ions in four ionic liquids: (a) $[\text{emim}]^+[\text{SCN}]^-$, (b) $[\text{emim}]^+[\text{N}(\text{CN})_2]^-$, (c) $[\text{emim}]^+[\text{C}(\text{CN})_3]^-$, (d) $[\text{emim}]^+[\text{B}(\text{CN})_4]^-$. The cation, anion and total charge density distributions are represented by red, green, and purple curves, respectively. Plots in the upper panels are the cases with the largest electrode charge Q_e 55
- 8.3 Electric potential $\Phi_{\text{total}}(z)$ in four ionic liquids. Top: $[\text{emim}]^+[\text{SCN}]^-$; second: $[\text{emim}]^+[\text{N}(\text{CN})_2]^-$; third: $[\text{emim}]^+[\text{C}(\text{CN})_3]^-$; bottom: $[\text{emim}]^+[\text{B}(\text{CN})_4]^-$. Blue: cathode, Yellow: anode. 57

8.4	Electrode charge Q_e and differential capacitances c as a function of $\Delta\Phi_{\text{half}}$, obtained in $[\text{emim}]^+[\text{SCN}]^-$, $[\text{emim}]^+[\text{N}(\text{CN})_2]^-$, $[\text{emim}]^+[\text{C}(\text{CN})_3]^-$, and $[\text{emim}]^+[\text{B}(\text{CN})_4]^-$	59
8.5	Differential capacitances c and differential capacitance of ionic layers(DCIL) c^1 , c^3 , and c^5 as a function of $\Delta\Phi_{\text{half}}$ in four ionic liquids: (a) $[\text{emim}]^+[\text{SCN}]^-$; (b) $[\text{emim}]^+[\text{N}(\text{CN})_2]^-$; (c) $[\text{emim}]^+[\text{C}(\text{CN})_3]^-$; (d) $[\text{emim}]^+[\text{B}(\text{CN})_4]^-$	61
8.6	Differential capacitances c , differential capacitance of ionic layers(DCIL) c^5 , and its divided components: c_{an}^5 and c_{cat}^5 as a function of $\Delta\Phi_{\text{half}}$ in four ionic liquids: (a) $[\text{emim}]^+[\text{SCN}]^-$; (b) $[\text{emim}]^+[\text{N}(\text{CN})_2]^-$; (c) $[\text{emim}]^+[\text{C}(\text{CN})_3]^-$; (d) $[\text{emim}]^+[\text{B}(\text{CN})_4]^-$	63
8.7	(a): Electrode charge Q_e and differential capacitances c as a function of $\Delta\Phi_{\text{half}}$, obtained in $[\text{emim}]^+[\text{SCN}]^-$. Q_e is compared with charge of ionic layers Q_{an}^5 and c is compared with differential capacitance of ionic layers c_{an}^5 , respectively. Maximum and minimum points of DC at negative potential are numbered. (b)-(d): Number density distribution $n_\alpha(z)$ of the ions near the cathode obtained in $[\text{emim}]^+[\text{SCN}]^-$. Black vertical line is the borderline between first and second ionic layers of which definition is explained in Supporting Information. As the cathode is more negatively charged, anions(coion) are expelled from the first ionic layer.	65
8.8	Fraction of anion component x_{an} as a function of $\Delta\Phi_{\text{half}}$, obtained in $[\text{emim}]^+[\text{SCN}]^-$, $[\text{emim}]^+[\text{N}(\text{CN})_2]^-$, $[\text{emim}]^+[\text{C}(\text{CN})_3]^-$, and $[\text{emim}]^+[\text{B}(\text{CN})_4]^-$ at 350K.	68

10.1	Differential capacitances c and differential capacitance of ionic layers(DCIL) c^1 , c^3 , and c^5 as a function of $\Delta\Phi_{\text{half}}$ in three ionic liquids: (a) $[\text{emim}]^+\text{BF}_4^-$; (b) $[\text{bmim}]^+\text{BF}_4^-$; (c) $[\text{hmim}]^+\text{BF}_4^-$.	73
10.2	Differential capacitances c , differential capacitance of ionic layers(DCIL) c^5 , and its divided components: c_{an}^5 and c_{cat}^5 as a function of $\Delta\Phi_{\text{half}}$ in three ionic liquids: (a) $[\text{emim}]^+\text{BF}_4^-$; (b) $[\text{bmim}]^+\text{BF}_4^-$; (c) $[\text{hmim}]^+\text{BF}_4^-$.	75
B.1	Thicknesses of ionic layers as a function of $\Delta\Phi_{\text{half}}$, obtained in $[\text{emim}]^+[\text{SCN}]^-$.	82

Chapter 1

Overview

1.1 Capacitors

Capacitor is an electric device which stores energy in electric field. Capacitance C is the ability of a capacitor to store charge Q with respect to electric potential V .

$$C = \frac{Q}{V} \quad (1.1)$$

The total energy W stored in the capacitor is

$$W = \int_0^Q V(q) dq = \int_0^Q \frac{q}{C} dq = \frac{Q^2}{2C} = \frac{1}{2} CV^2 \quad (1.2)$$

Capacitor with larger capacitance stores more energy when the electric potential V is given. Dielectric materials are commonly inserted in between two electrodes to enlarge the capacitance. Such capacitor store more charge because dielectric molecules in Figure 1.1 are polarized and the electric field of the electrode is weakened.

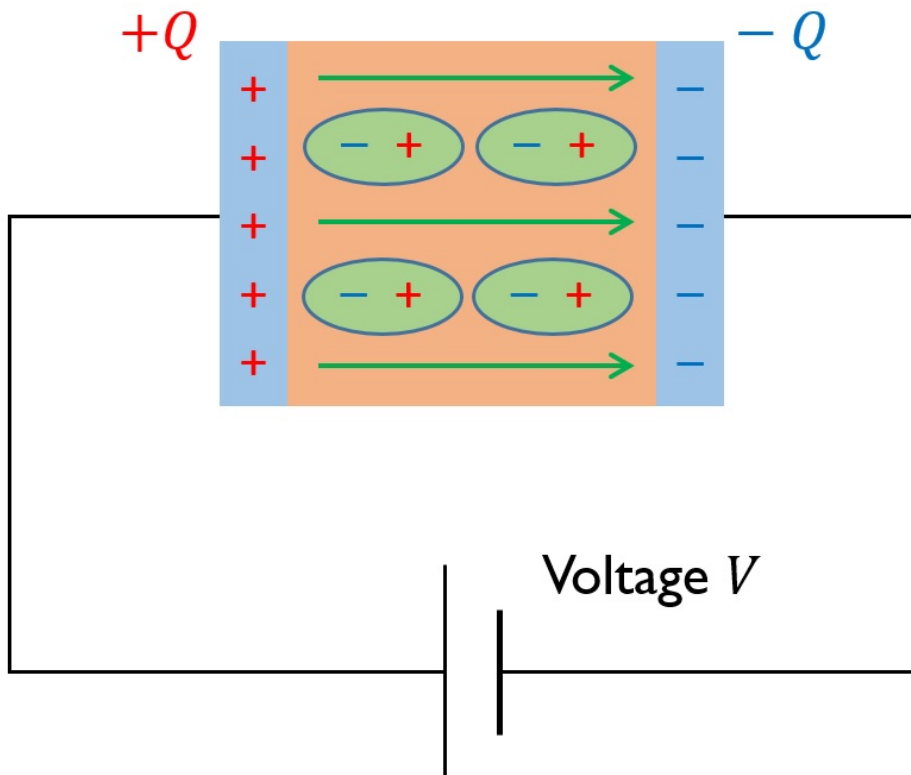


Figure 1.1: Schematic representation of a capacitor with dielectric material. Red: positive charge, Blue: negative charge, Green: electric field line, Orange: dielectric material.

1.2 Electric double layer capacitors

Electric double layer capacitor(EDLC) is a noble class of supercapacitors which have 10 to 100 times capacitance as conventional capacitor.^[1] When electrolytes are inserted in place of dielectric material, mobile ions are rearranged. Alternating layers of counterions and coions, electric double layer(EDL) is formed near a charged electrode.[Figure 1.2] The size of EDLCs can be reduced up to nanometer scales as the EDL efficiently screens the electric field only in 20-30 Å from the electrode. As the EDL structure changes with respect to the electric potential, capacitance is also a function of electric potential. Differential capacitance(DC) c thus has been measured and studied for EDLC systems.

$$c = \frac{\partial Q}{\partial V} \quad (1.3)$$

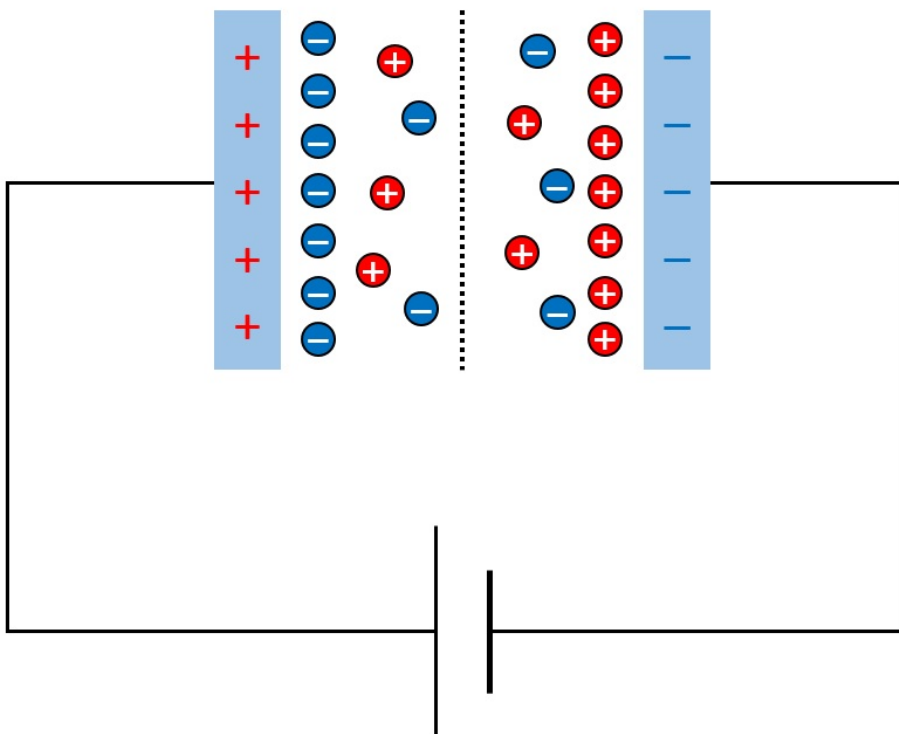


Figure 1.2: Schematic representation of an electric double layer capacitor. Counterions are accumulated near charged electrodes. Red: positive charge, Blue: negative charge.

1.3 Shape of DC curves

The dependence of differential capacitance on electric potential has been widely investigated for EDLC systems. Theoretical studies have given different explanations of DC behaviors as a function of electric potential. Mean field theory introduced the lattice saturation effect^[2-4] in which capacitance decreases at high potential region because electric double layer is thickened. DC behavior at intermediate potential is dependent on ion concentration. In the case of low concentration ions are actively rearranged at intermediate potential and capacitance increases. Two maxima of camel-shaped DC curve^[5-14] are formed at positive and negative potentials. At high ion concentration DC curve is bell-shaped^[5-7,15-17]. The capacitance monotonically decreases from the potential of zero charge(PZC) because the ion rearrangement at intermediate potential is insignificant. An alternative explanation of camel-shaped DC is provided by Monte Carlo simulation study with coarse-grained model of ILs.^[6,18] Charge neutral chains of cations aggregate each other and form “latent voids” at low potential. Charged beads replace latent voids at intermediate potential and capacitance maxima are generated. Additionally, self-consistent mean field theories state that camel-shaped DC curve is a consequence of higher permittivity near a charged electrode.^[5,8]

1.4 Ionic liquids

Ionic liquids(ILs) are organic salts which are in the liquid phase without any solvents. They have been proposed as environmentally benign solvents because they have negligible vapor pressures, they solvate both polar and non-polar solutes, and they are easy to recycle. Due to their wide electrochemical window and high ion conductivity, ionic liquids have attracted various electrochemical applications, namely electrodeposition, batteries, dye-sensitized solar cells, and supercapacitors.^[19] Another notable characteristic of ILs is various combinations of cations and anions.^[20] Chemical structure of ion has been systematically tuned and its effect on liquid properties has been widely investigated.

Part I

Effects of Alkyl Chain Length in Cation on Interfacial Structure and Differential Capacitance

Chapter 2

Introduction

Room-temperature ionic liquids (RTILs) have unique physicochemical properties such as high ion conductivity, high electrochemical and thermal stability, which allows superior performance over conventional solvents for electrochemical applications.^[21] In the past decades, RTILs have been investigated as key solvents for electrodeposition, batteries, supercapacitors, and dye-sensitized solar cells.^[19] Interfacial properties of the RTILs are one of the most important factors for their surface-dependent electrochemical applications. A number of experimental and computational efforts have been made to obtain insights on their interfacial behaviors. Recent theoretical and computational studies of the interfacial systems^[5-9,22-34] have offered a microscopic understanding on the electric double layer structure and associated dynamics, and capacitive properties of RTILs as electrolytes in electric double layer capacitors (EDLCs).

Electrode as well as electrolyte plays an important role in building EDLCs. A wide variation of carbon-based materials have been proposed and applied as electrodes. Graphene, a planar allotrope of carbon, has drawn

considerable attention since its discovery because it is chemically stable and mechanically flexible, and has large surface area and high conductivity of heat and electron.^[35] Especially, extensive computational research has been dedicated to graphene due to its well-defined chemical structure.^[36]

Many studies on EDLCs have devoted their attention to the shape of the differential capacitance curve with respect to the applied electrode potential for RTIL electrolytes. Experimental and theoretical studies have characterized capacitance behaviors of the RTILs as either camel-shaped^[5-14] or bell-shaped^[5-7,15,16] differential capacitance (DC) curves. A “lattice saturation effect”^[2-4] on the capacitance was taken into account such that an electric double layer becomes thicker and thus the capacitance decreases with the electrode potential increasing. This accounts for the decreasing capacitance behavior from the local maxima in DC curves for RTILs. The potential difference between the local maxima in the camel-shaped capacitance curve becomes narrower with increasing ion concentration, resulting in a transition into a bell-shaped one at which the maximum occurs at potential of zero charge (PZC). On the other hand, Monte Carlo simulation studies reported a camel-shaped DC for a coarse-grained model of RTILs with neutral chain.^[6,18] Neutral beads in cations first act as “latent voids” at low electrode potentials, and are replaced by charged beads at moderate electrode potentials.^[18] In addition, a self-consistent mean field model was developed in which the permittivity depending on the distance from the electrode surface is responsible for the camel-shaped capacitance curve.^[5,8]

Experimental measurements on DCs for EDLCs have provided diverse results even though the same ionic species and electrodes are considered. For example, for the imidazolium-based tetrafluoroborate RTILs, U-shaped

DC curves were observed at glassy carbon and highly oriented pyrolytic graphite (HOPG) electrodes,^[37,38] while camel-shaped DC curves at glassy carbon electrodes were found.^[10] On the other hand, bell-shaped DC curves were observed for 1-butyl-3-methylimidazolium tetrafluoroborate at the gold electrode.^[15] Molecular dynamics (MD) simulation studies on DC curve in RTILs have also been reported for the graphite electrodes. A U-shaped capacitance curve was observed over a limited potential range of -1.5 1 V in 1-butyl-3-methylimidazolium nitrate,^[23] while camel-shaped capacitance curves were found in alkyylimidazolium RTILs with a hydrophobic bis(trifluoromethanesulfonyl)imide ([TFSI]⁻) anion.^[7,14]

Differential capacitance is affected by various factors such as effective permittivity and dispersion force in RTILs,^[6,39] topology and material of electrodes.^[7,12,14,31,40-45] Among other things, the alkyl chain length in imidazolium-based cations of RTILs can have a great influence on electrolyte properties for EDLCs such as viscosity, conductivity and capacitance. On the whole, as the alkyl chain becomes longer, the viscosity gets larger while the conductivity smaller in imidazolium-based RTILs due to an enhanced steric hindrance.^[14] It was found that RTIL electrolytes with longer alkyl chain length provide lower differential capacitances for various electrodes.^[14,16] Although there have been numerous studies on RTIL-electrode interfacial systems, microscopic understanding of the capacitance behavior of the system is far from clear. In this article, we pay attention to the effect of the alkyl chain on structure and differential capacitance at the graphene electrode, employing various imidazolium-based RTILs with tetrafluoroborate anion.

The outline of this part is as follows: We first give in Chapter 3 a brief

description of the model system and simulation methods employed in this part. MD results are compiled in Chapter 4, where interfacial structures and differential capacitances of EDLC systems, comprising two graphene sheets and 1-C_n(n=2,4,6)-3-methylimidazolium tetrafluoroborate ionic liquids, are analyzed to examine their variations with alkyl chain length. Concluding remarks are given in Chapter 5.

Chapter 3

Models and Methods

The simulation cell comprised 256 pairs of an imidazolium-based RTIL confined between the parallel graphene plates [Figure 3.1]. Three different RTILs, 1-ethyl-3-methylimidazolium tetrafluoroborate ($[\text{emim}]^+\text{BF}_4^-$), 1-butyl-3-methylimidazolium tetrafluoroborate ($[\text{bmim}]^+\text{BF}_4^-$) and 1-hexyl-3-methylimidazolium tetrafluoroborate ($[\text{hmim}]^+\text{BF}_4^-$) were employed as RTILs. Each electrode was modeled as a rigid and flat layer of 448 sp^2 -hybridized carbon atoms, i.e., a single graphene sheet, with dimensions $34.3 \times 34.0 \text{ \AA}^2$. For convenience, we employed a Cartesian coordinate system, where the graphene electrodes at $z = \pm z_0$ span the xy -plane ($-x_0 < x < x_0$, $-y_0 < y < y_0$) and its normal defines the z -direction. Electrode separation d ($= 2z_0$) was fixed to be 66 \AA for $[\text{emim}]^+\text{BF}_4^-$ of which density was determined previously using NPT ensemble simulation at 350 K and 1 atm.^[29] Electrode separations for the other two RTILs were adjusted to reproduce the ratios in their experimental bulk densities,^[46–48] the values of which are 78 and 91 \AA for $[\text{bmim}]^+\text{BF}_4^-$ and $[\text{hmim}]^+\text{BF}_4^-$, respectively. Flexible all-atom force fields^[49,50] were used for cations. Partial charge and

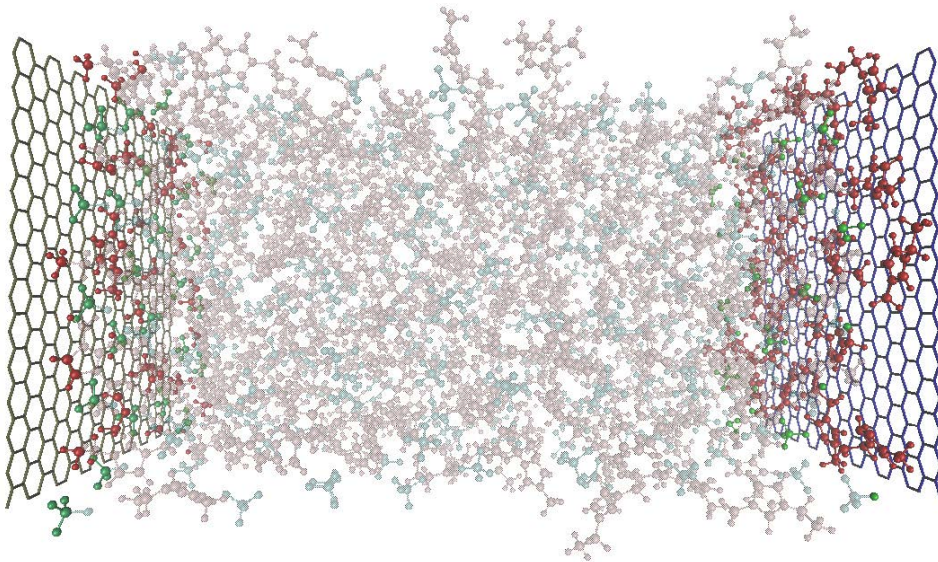


Figure 3.1: Snapshot of one of our systems. Yellow: anode with charge $Q_e = +8e$, Blue: cathode with the opposite charge, Red: $[\text{emim}]^+$ cation, Green: BF_4^- anions. Ions in the interfacial layers are highlighted. We can see that a charged electrode attracts counterions and expels coions.

force field description for BF_4^- anion were taken from the ref46 and47, respectively. Surface charge densities at the electrodes were varied in the total charge Q_e from 0 to $\pm 8.5 e$, with a uniform increment of $0.5 e$, where e is an elementary charge. Electronic polarizability for both the graphene and electrolytes was ignored in our present study.^[26] The Lennard-Jones parameters employed for C atoms of the graphene were $\epsilon = 43.2$ K and $\sigma = 3.4$ Å.^[51] During the simulations, the graphenes were held rigid with carbon-carbon bond length of 1.42 Å.

All production runs were conducted with Nosé-Hoover thermostat at 350 K using the GROMACS program.^[52] The long-range electrostatic interactions were computed via the Particle Mesh Ewald method with correction for slab geometry,^[53] resulting in essentially no truncation of these interactions. The trajectories were integrated via the Verlet leapfrog algorithm using a time step of 1 fs. Five independent equilibrium simulations were carried out with 10 ns equilibration, followed by a 10 ns production run from which ensemble averages were computed.

Chapter 4

Results and Discussion

4.1 Interfacial Structure

We examine the structure of RTILs confined between two parallel graphene electrodes. Number density distribution $n_\alpha(z)$ of center of mass of the ion species α defined by

$$n_\alpha(z) = A_0^{-1} \int_{-x_0}^{x_0} \int_{-y_0}^{y_0} dx' dy' n_\alpha(x', y', z); A_0 = 4x_0y_0 \quad (4.1)$$

was calculated, where A_0 is the surface area of the graphene electrode. The average ion densities $n_\alpha(z)$ according to variations with alkyl chain are displayed in Figure 4.1. We first consider the results for [emim]⁺BF₄⁻ [Figure 4.1 (a)]. Cations and anions make a strong solvent layer in a distance of $\Delta z \leq 6$ Å from the electrode surface, followed by a significant fluctuation along z , regardless of the electrode charge density. This indicates that on average ions form layered structures near flat surfaces.^[7,9,23,25,26,33,34,54–56] For the neutral charge density with $Q_e = 0$ in the bottom panel, the maximum distributions for [emim]⁺ and BF₄⁻ ions in the first solvent layer occur at z

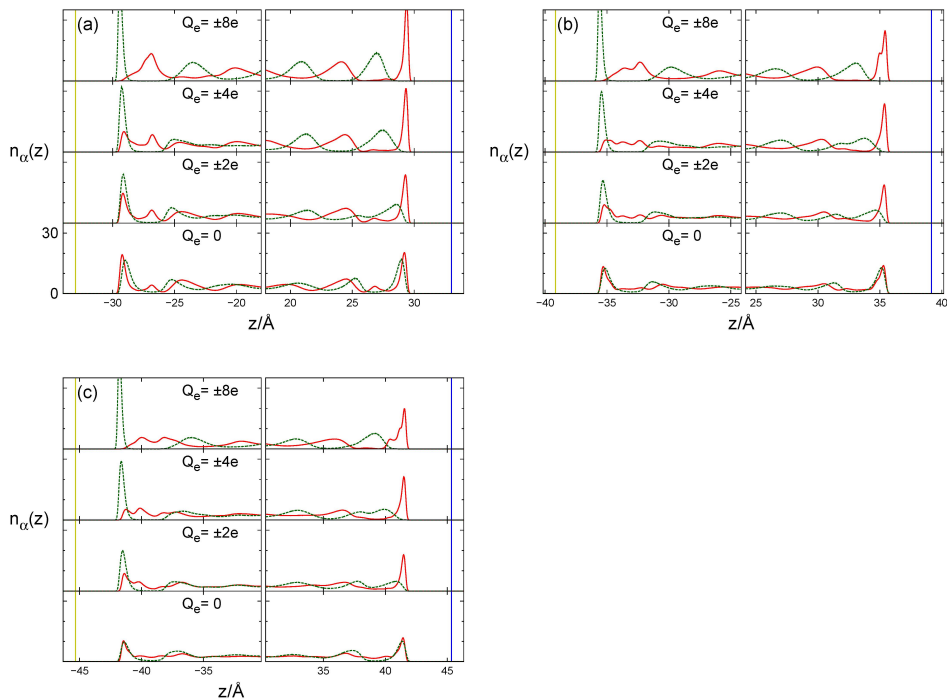


Figure 4.1: Number density distribution functions $n_\alpha(z)$ of cations and anions in three RTILs; (a) $[\text{emim}]^+\text{BF}_4^-$; (b) $[\text{bmim}]^+\text{BF}_4^-$; (c) $[\text{hmim}]^+\text{BF}_4^-$. The cation and anion number density distributions are represented by red and green curves, respectively. The locations of the electrode are indicated by yellow blue (anode) and blue (cathode) vertical lines. Counterions are abundant in the first layer of a charged electrode. Plots are shifted up as total electrode charge Q_e increases from the bottom to the top panel.

= 3.8 and 4.0 Å. The cation is located slightly closer to the electrode due to the π -stacking formation between the cation and the electrode.^[28,57] Similar features are exhibited also in $n_\alpha(z)$'s of [bmim]⁺BF₄⁻ and [hmim]⁺BF₄⁻ in Figure 4.1 (b) and (c). Imidazolium-based cation has a better affinity to the graphene electrode compared to BF₄⁻ anion.

For the charged electrodes cases, $n_\alpha(z)$ in [emim]⁺BF₄⁻ are also shown in Figure 4.1 (a). As the electrode becomes more positively charged, the first peak in the solvent layers by BF₄⁻ becomes higher and narrower at $\Delta z = 3.6$ Å, while [emim]⁺ at $\Delta z \leq 5$ Å are gradually expelled from the anode and move into the second peak of the double-layered first shell. Beyond the total charge $Q_e \geq 7e$, the first single solvent layer by [emim]⁺ is built up distinctively from that by BF₄⁻, generating an alternating structure between the cations and anions. In the opposite case for the negatively-charged electrodes, *i.e.*, cathodes, as we increase the electrode charge density, the first solvent layer structure by [emim]⁺ becomes stronger without change of their maximum location, followed by forming the solvent layers by anions. However, larger cations, especially [hmim]⁺, make a double-layered structure in the first solvent shell for the negatively-charged electrodes. This is due to their steric effect exerted by larger cations. Analogous to the interfacial structures between the anode and cations, anion structure at the cathode becomes weaker and more distant with increase of the electrode charge.

To gain more insight into the interfacial solvent layer, orientations of the cations to the electrode surface are analyzed. Probability distributions $P(\theta_c)$ of the chain angle θ_c between the surface normal vector and alkyl chain vector of the cation in the first solvent layer were examined. A schematic illustration is presented in Figure 4.2: the chain vector is defined as one

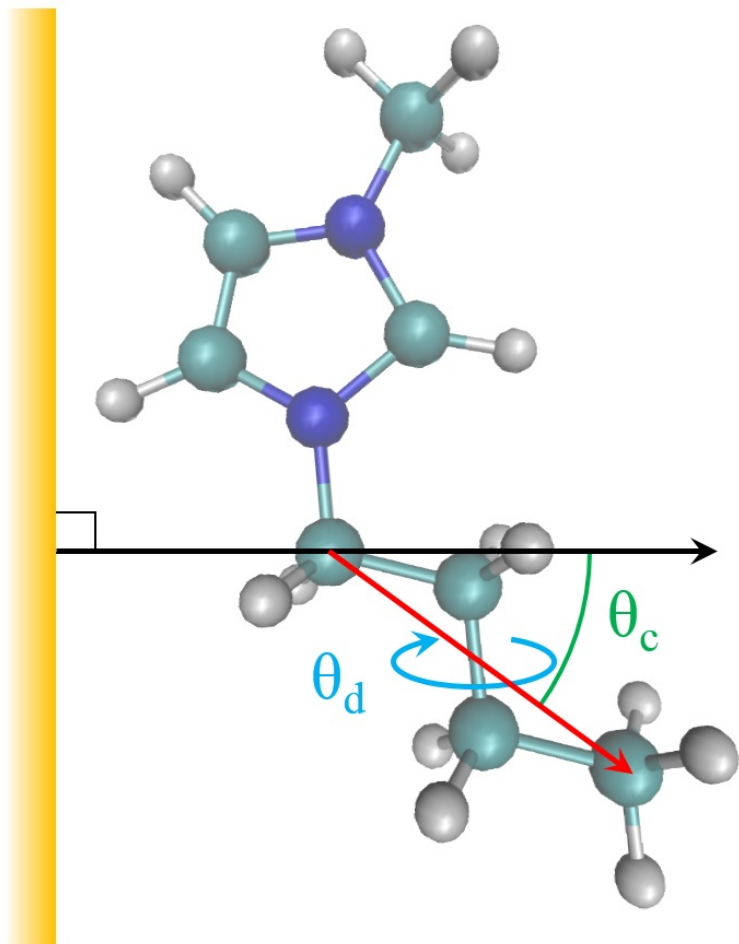


Figure 4.2: Schematic representation of the chain angle θ_c and the dihedral angle θ_d in $[\text{bmim}]^+$. Yellow: graphene electrode, Black: surface normal vector, Red: chain vector, Green: chain angle θ_c , Blue: dihedral angle θ_d .

from the carbon connected to the imidazolium ring to the terminal methyl carbon. The angle distributions $P(\theta_c)$ obtained in three RTILs are displayed in Figure 4.3. Regardless of the electrode charge density, the maximum position of $P(\theta_c)$ occurs at about 90° because cations tend to align in parallel to the electrode surfaces. As we increase alkyl chain length from $[\text{emim}]^+$ to $[\text{hmim}]^+$, the peak distribution in $P(\theta_c)$ becomes higher and narrower. This reveals that π -stacking of the imidazolium ring^[57] and parallel alignment of the alkyl chain to electrode represent the most probable orientation of cations in the interfacial region.^[58]

To reveal interfacial orientations of $[\text{bmim}]^+$ and $[\text{hmim}]^+$ more clearly, probability distributions $P(\theta_d)$ of dihedral angles for alkyl chains were also calculated in the first solvent layers and, compared to those in bulk. Figure 4.4 (a) and (b) show $P(\theta_d)$ obtained in $[\text{bmim}]^+\text{BF}_4^-$ and $[\text{hmim}]^+\text{BF}_4^-$, respectively. We note that $[\text{bmim}]^+$ and $[\text{hmim}]^+$ prefer an anti conformation, that is, an extended structure of the alkyl chain, to a gauche conformation, regardless of the electrode charge density. This supports an idea that our alkyimidazolium cations orient almost in parallel with graphene electrodes, which is consistent with experimental studies with carbon^[58] and gold electrodes.^[59] Snapshots in Figure 4.5 show representative configurations of cations in the first solvent layers in the presence of neutral electrodes.

Turning to $P(\theta_c)$ in Figure 4.3, we examine the chain angle distribution with respect to electrode charge. As the anode becomes more positive, all three cations show broader distributions in $P(\theta_c)$. Because cations tend to be expelled from the anode as shown in Figure 4.1, the orientation of the alkyl chain is much less influenced by confinement. On the other hand,

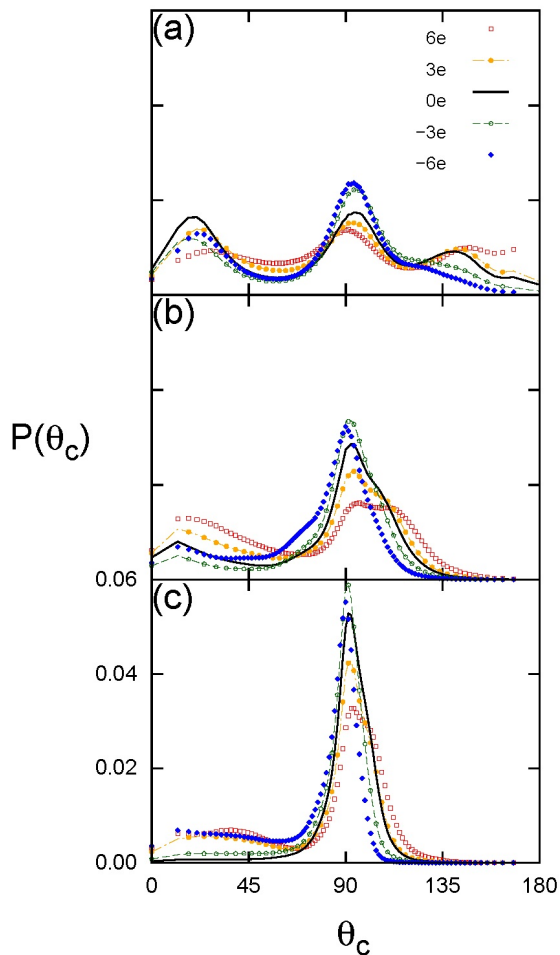


Figure 4.3: Angle probability distributions $P(\theta_c)$ between the surface normal vector and alkyl chain vector of the cation, obtained in (a) $[\text{emim}]^+\text{BF}_4^-$, (b) $[\text{bmim}]^+\text{BF}_4^-$ and (c) $[\text{hmim}]^+\text{BF}_4^-$ at 350K. The chain vector is defined as one from the carbon connected to the imidazolium ring to the terminal one and their normalization satisfies $\int_0^\pi P(\theta_c)\sin\theta_c d\theta_c = 1$.

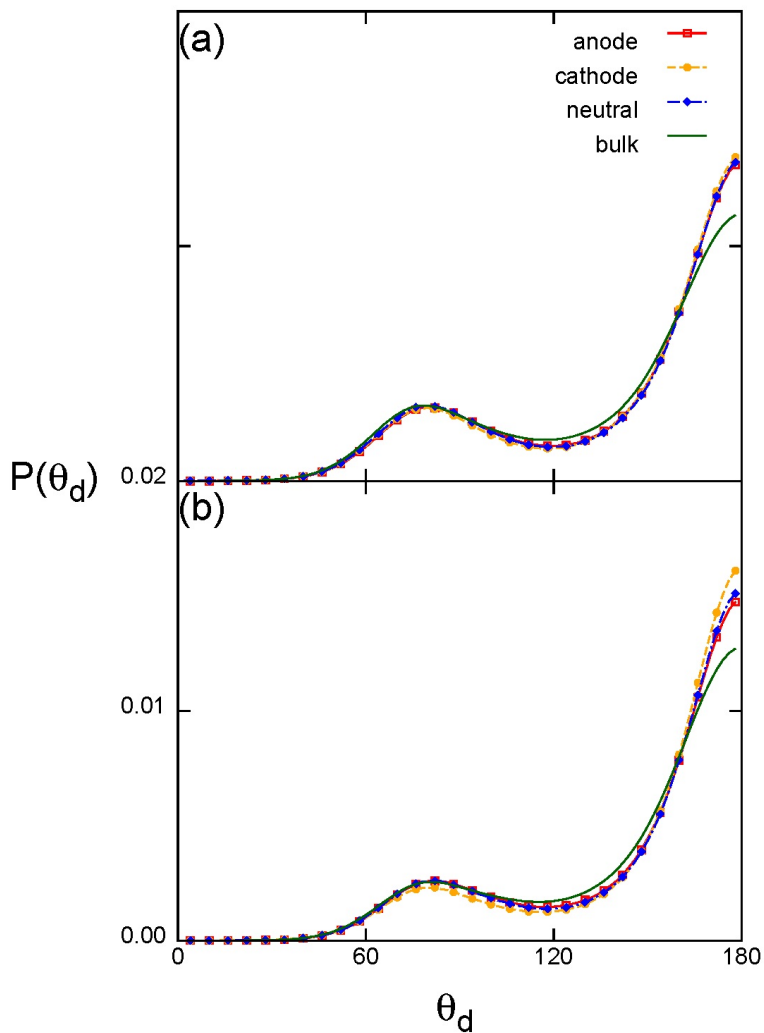


Figure 4.4: Probability distributions $P(\theta_d)$ of the dihedral angle in the alkyl chain connected to the nitrogen of the imidazolium ring in (a) $[\text{bmim}]^+\text{BF}_4^-$ and (b) $[\text{hmim}]^+\text{BF}_4^-$ at 350K. Results for cathode and anode were obtained with $Q_e = \pm 2e$. $P(\theta_d)$ is normalized by $\int_0^{2\pi} P(\theta_d)d\theta_d = 1$.

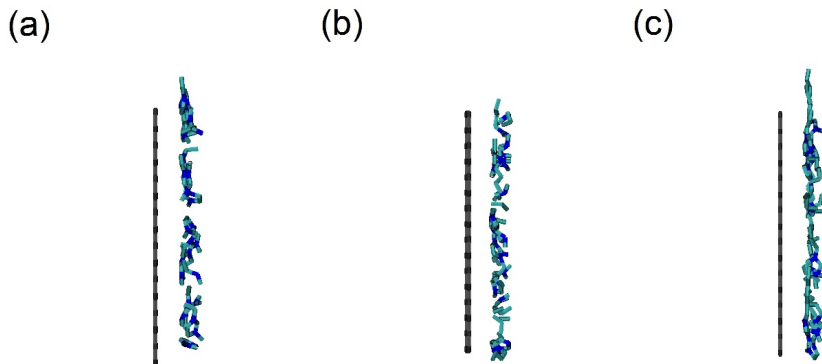


Figure 4.5: Snapshots of alkylimidazolium cations in the first solvent layer from the neutral electrodes, obtained in (a) $[\text{emim}]^+\text{BF}_4^-$, (b) $[\text{bmim}]^+\text{BF}_4^-$, and (c) $[\text{hmim}]^+\text{BF}_4^-$ at 350 K.

electrostatic interaction and π -stacking make strong confinement of cations near cathode and the parallel alignment of alkyl chains are more favored. The distribution of parallel orientations at $\sim 90^\circ$ is enhanced while $P(\theta_c)$ in other regions diminish as the cathode becomes more negative. Such dependences are more profound in the cation with longer alkyl chain. $[\text{emim}]^+$ show another peak structures in $P(\theta_c)$ at $20\text{-}30^\circ$ and $140\text{-}160^\circ$ with smaller probabilities besides the dominant orientations around 90° . As the anode becomes more positive, cations show broad distributions in $P(\theta_c)$ beyond the region of $80\text{-}120^\circ$. On the other hand, as the cathode becomes more negative, the distribution of parallel orientations at $\sim 90^\circ$ is enhanced while $P(\theta_c)$ decreases in the region of $120\text{-}160^\circ$. For $[\text{bmim}]^+$ and $[\text{hmim}]^+$ in Figure 4.3 (b) and (c), $P(\theta_c)$ at $\theta_c \geq 130^\circ$ tends to diminish and the alkyl

chains of them aligns toward the liquid region rather than toward the electrode surface, except that main parallel orientations. This is attributed to steric effect by alkyl chain caused by strong π -stacking formation of the imidazolium ring in the confined system. Another noteworthy feature is that $P(\theta_c)$ for [hmim]⁺ has a considerable distribution in the region of 30-60° even for the highly charged cathode ($Q_e \leq -6e$) and exhibits a shoulder structure. This arises from the double-layered structure in the first solvent layer of [hmim]⁺ ions [Figure 4.1 (c)] near the electrode with highly positive surface charge.

4.2 Electric Potentials and Differential Capacitances

Average charge density distribution $\rho_\alpha(z)$ is considered as

$$\rho_\alpha(z) = A_0^{-1} \int_{-x_0}^{x_0} \int_{-y_0}^{y_0} dx' dy' \rho_\alpha(x', y', z), \quad (4.2)$$

where $\rho_\alpha(x', y', z)$ is the local charge density arising from the atomic charge distribution of ionic species α . The results for $\rho_\alpha(z)$ in three RTILs are exhibited in Figure 4.6. Close to the electrode, both cation and anion charge densities show rapid oscillations, which disappear in within 10 Å. This multiple charge layered structure is coincident with results obtained in different RTILs.^[7,9,12-14,25,27,60,61] It is notable that the average charge density converges to the plateau faster, compared to layering structures of the ions in $n_\alpha(z)$.

An electric potential between two parallel electrodes is calculated by

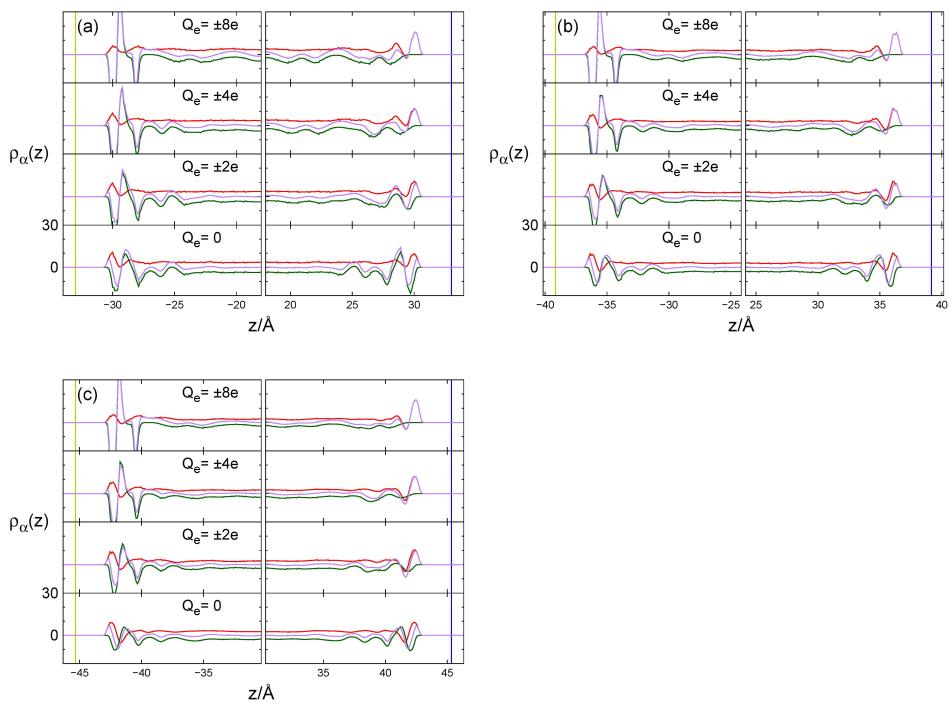


Figure 4.6: Charge density distribution functions $\rho_\alpha(z)$ in three RTILs; (a) $[\text{emim}]^+\text{BF}_4^-$; (b) $[\text{bmim}]^+\text{BF}_4^-$; (c) $[\text{hmim}]^+\text{BF}_4^-$. The cation, anion and total charge density distributions are represented by red, green, and purple curves, respectively. Plots are shifted up as total electrode charge Q_e increases from the bottom to the top panel.

integration of Poisson equation,

$$\Phi_{\alpha}(z) = -4\pi \int_0^z dz'(z - z')\rho_{\alpha}(z'), \quad (4.3)$$

where $\rho_{\alpha}(z)$ is the average charge density obtained in Eq. (4.2). Total electric potential between the electrodes, considered as

$$\Phi_{\text{total}}(z) = \Phi_{\text{cation}}(z) + \Phi_{\text{anion}}(z) + \Phi_{\text{electrode}}(z), \quad (4.4)$$

are shown in Figure 4.7 for three RTILs. Noteworthy is that potentials of zero charge (PZC) with respect to the bulk region turn out to be positive for three RTILs. This is consistent with our previous studies.^[28] The interfacial configuration [Figure 4.1] of cations adjacent to the electrode gives rise to their higher number density and thus larger affinity compared to BF_4^- ions. This feature was ascribed to the π -stacking structure between the imidazolium ring and graphene surface.^[57] The PZC increases with alkyl chain length, and the obtained values are 0.11, 0.19 and 0.26 V for $[\text{emim}]^+\text{BF}_4^-$, $[\text{bmim}]^+\text{BF}_4^-$ and $[\text{hmim}]^+\text{BF}_4^-$, respectively. It discloses that three imidazolium cations have greater affinity than BF_4^- , the extent of which becomes the most considerable in $[\text{hmim}]^+$.

For the charged electrodes, $\Phi_{\text{total}}(z)$ rapidly drops $\Delta z \leq 4 \text{ \AA}$ and becomes essentially constant for $\Delta z \geq 20 \text{ \AA}$. Indicating that RTIL ions form effectively an electric double layer within $\Delta z \leq 20 \text{ \AA}$ and efficiently screens the electric field generated by the electrode surface charges. The $\Delta\Phi_{\text{tot}}$ is divided into anodic and cathodic potential difference of half cells $\Delta\Phi_{\text{half}}$ with respect to PZC.

$$\Delta\Phi_{\text{half}} = \Phi_{\text{electrode}} - \Phi_{\text{bulk}}, \Delta\Phi_{\text{tot}} = \Delta\Phi_{\text{half}}^{(+)} - \Delta\Phi_{\text{half}}^{(-)}, \quad (4.5)$$

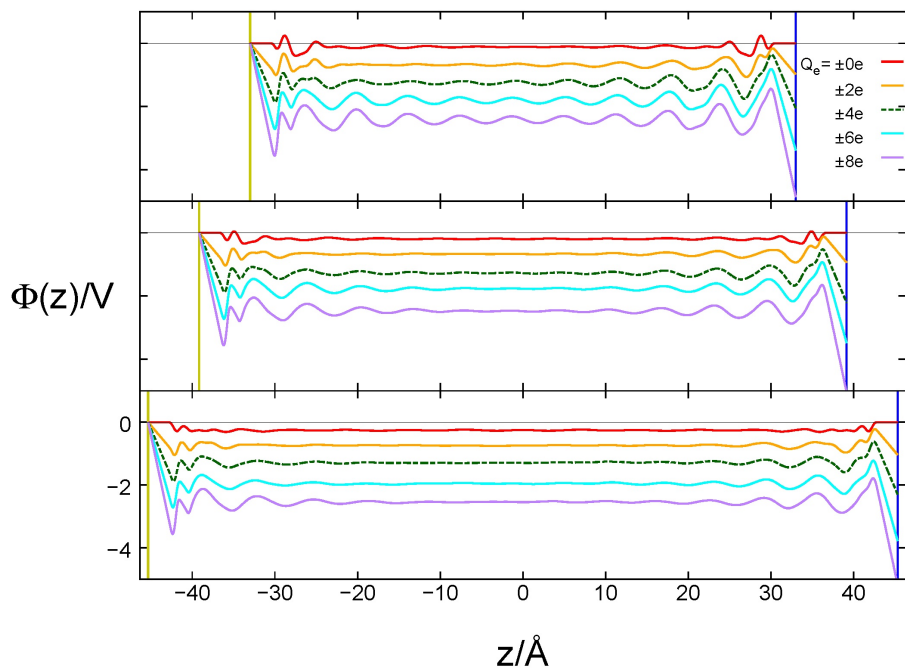


Figure 4.7: Electric potential $\Phi_{\text{total}}(z)$ in three RTILs; top: [emim]⁺BF₄⁻; middle: [bmim]⁺BF₄⁻; bottom: [hmim]⁺BF₄⁻. Yellow: anode, Blue: cathode.

In the inset of Figure 4.8, $\Delta\Phi_{\text{half}}$ increases almost linearly with electrode surface charge. Nonetheless, we focus on their differential behavior of surface electrode charge as a function of $\Delta\Phi_{\text{half}}$, that is, differential capacitance (DC) c defined as

$$c = \frac{\partial Q_e}{A_0 \partial \Delta\Phi_{\text{half}}} \quad (4.6)$$

The differential capacitances were evaluated by the analytical derivative of the parabola fits for $Q_e - \Delta\Phi_{\text{half}}$ plots, considering 29 windows with 7-9 data points in $\Delta\Phi_{\text{half}}$. The DC curves for three systems are shown in Figure 4.8. We find that all three RTILs provide a bell-shaped DC curve, in which c monotonically decreases with increase of $\Delta\Phi_{\text{half}}$. This is an outstanding characteristic in RTILs for EDLCs, accounted by ‘‘lattice saturation’’^[2-4] with increasing the electrode potential. This accounts for the decreasing capacitance behaviors from the local maxima in DC curves for RTILs. Our results agree with both theoretical studies of model systems^[5,6] and experimental studies on systems with alkyimidazolium cation.^[15,16] On the other hand, camel-shaped curves have also been reported in other studies.^[6-14] Difference between the ion densities associated with temperature may give rises to the discrepancy.^[44] Electronic polarizability of the electrode ignored in our study can be also one of the factors to explain the discrepancy as a missing nonlinear behavior occurring in their electric double layers for small electrode potentials.^[62,63]

We examine the influence of the alkyl chain length on capacitance. The maximum c occurring around PZC is found to decrease as the chain length increases. This is in accordance with recent experimental findings that specific capacitance depends on the size of both cations and anions and decreases with increasing the ion size.^[10,16] The corresponding value of $\Delta\Phi_{\text{half}}$

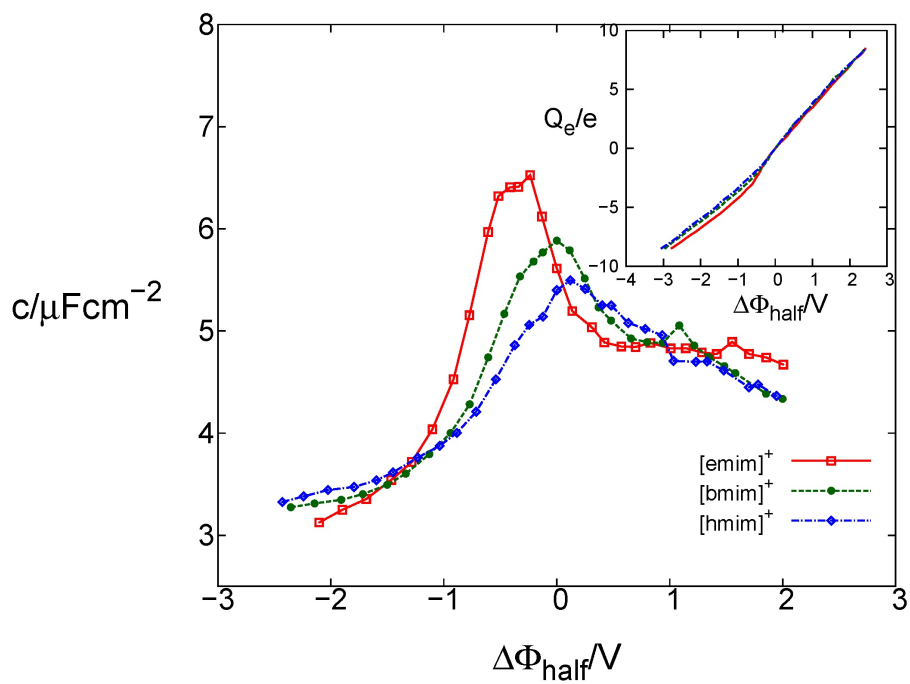


Figure 4.8: Differential capacitances c and electrode charge Q_e as a function of $\Delta\Phi_{\text{half}}$, obtained in $[\text{emim}]^+\text{BF}_4^-$, $[\text{bmim}]^+\text{BF}_4^-$ and $[\text{hmim}]^+\text{BF}_4^-$ at 350K.

shifts from the negative to the positive: -0.24, 0 and 0.12 V for [emim]⁺BF₄⁻, [bmim]⁺BF₄⁻ and [hmim]⁺BF₄⁻, respectively. The cathodic capacitances of three systems decrease fast as the cathode is more highly charged. At high negative potential ($\Delta\Phi_{\text{half}} < -1.3$ V), the relation between capacitance and alkyl chain length is reversed: RTIL with longer alkyl chain shows larger capacitance.

An anodic capacitance is slightly higher than cathodic one in [bmim]⁺BF₄⁻ and [hmim]⁺BF₄⁻. This feature between the cathodic and anodic capacitances was also found in other RTILs.^[37,64] On the average, BF₄⁻ anions better shield the anode over the wide range of $\Delta\Phi_{\text{half}}$ due to their smaller ion size compared to [bmim]⁺ and [hmim]⁺. This is also found in [emim]⁺BF₄⁻ for the moderate and high $\Delta\Phi_{\text{half}}$. However, in the range of small $\Delta\Phi_{\text{half}}$ ($-0.5\text{V} \leq \Delta\Phi_{\text{half}} \leq 0$), [emim]⁺BF₄⁻ gives exclusively high cathodic capacitance; even higher than anodic counterpart. This finding is somewhat surprising considering efficiency in screening associated with their ion size: the cation is bigger than the anion. Ref30 has shown explicitly the screening ability of each ion separately in ionic liquid EDLC systems. For small cathodic $\Delta\Phi_{\text{half}}$, the screening efficiency arising from the π -stacking of the imidazolium ring becomes more prominent in [emim]⁺BF₄⁻.

4.3 Ion Accumulation in the Interfacial Layer

The bell-shaped behavior of DC has two major aspects: ‘single maximum’ and the ‘lattice saturation’. To understand DC behaviors according to the $\Delta\Phi_{\text{half}}$, we consider the ion number difference ΔN in the first layer defined

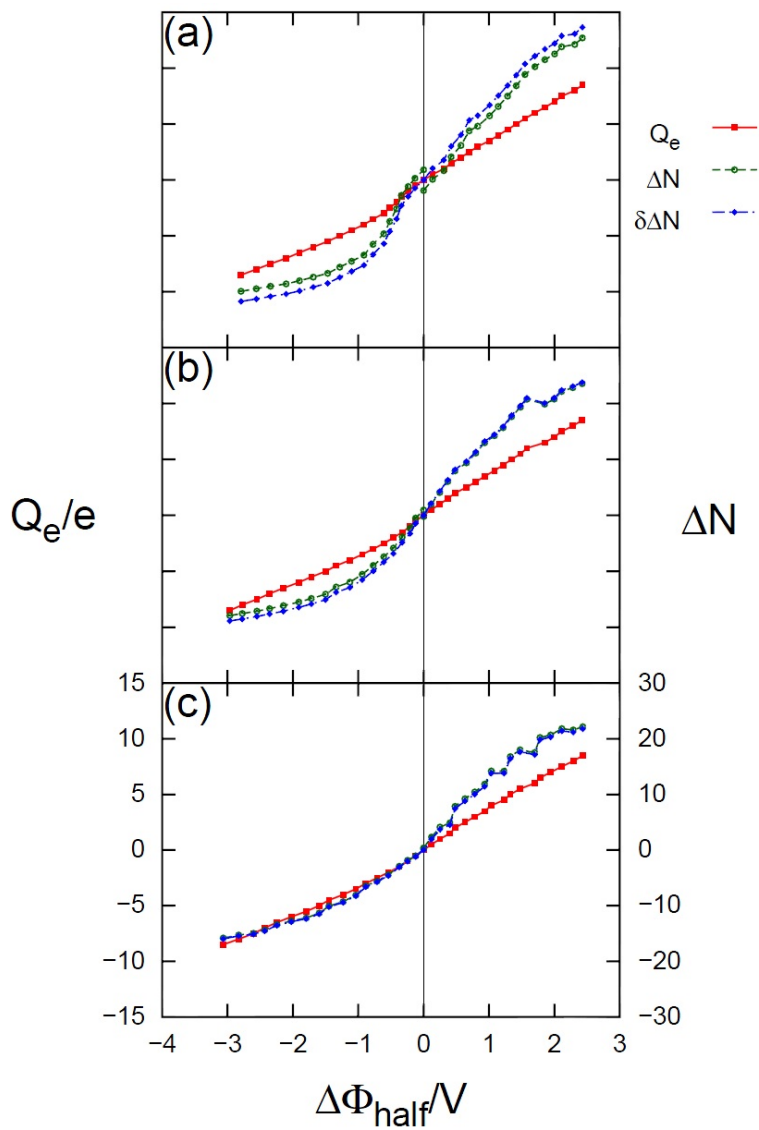


Figure 4.9: Electrode charge Q_e and ion number difference ΔN in three RTILs; (a) $[\text{emim}]^+\text{BF}_4^-$; (b) $[\text{bmim}]^+\text{BF}_4^-$; (c) $[\text{hmim}]^+\text{BF}_4^-$. ΔN has two values at $\Delta\Phi_{\text{half}} = 0$.

as

$$\Delta N = N_{\text{anion}} - N_{\text{cation}}; N_{\alpha} = A_0 \int_{\text{electrode}}^{\text{first layer}} dz' n_{\alpha}(z'), \quad (4.7)$$

which has similar dependence with that of Q_e : monotonic increase with electrode potential. The ΔN and Q_e are displayed in Figure 4.9. The fact that ΔN is comparable to twice Q_e for all charged electrodes confirms overscreening behavior by effective counter-ions in the first layer, followed by compensations of the alternating layers.^[65]

Employing this new property in place of Q_e , we follow the same analysis protocol. We define differential ion capacity (DIC) R in the first layer as

$$R = \frac{\partial \delta \Delta N}{\partial \Delta \Phi_{\text{half}}}, \quad (4.8)$$

and compare with DC for each kind of systems in Figure 4.10 (b)-(d). As we can see from Figure 4.9, ΔN is not uniquely defined at zero potential. We thus introduced $\delta \Delta N$ for smooth differentiation, of which definition is explained in Appendix A. The location and the width of peaks show good match between DC and DIC for $[\text{bmim}]^+$ and $[\text{hmim}]^+$ systems. The decreasing patterns from the maximum are also similar to each other. Especially, short increases at +1.1 V in $[\text{bmim}]^+$ system [Figure 4.10 (c)] and ruggedness of curves in $[\text{hmim}]^+$ system [Figure 4.10 (d)] are outstanding. We infer from these consistencies that the first feature of bell-shaped DC is generated by the ion accumulation in the nearest layer.

The “lattice saturation” effect on DIC is less pronounced than on DC. The former changes upon electrode potential more drastically than the latter, and the range of potential that the changes occur is broader in the former. There must be some other effects in action to generate the “lattice saturation” effect. Screening by further layers is a probable candidate.^[30]

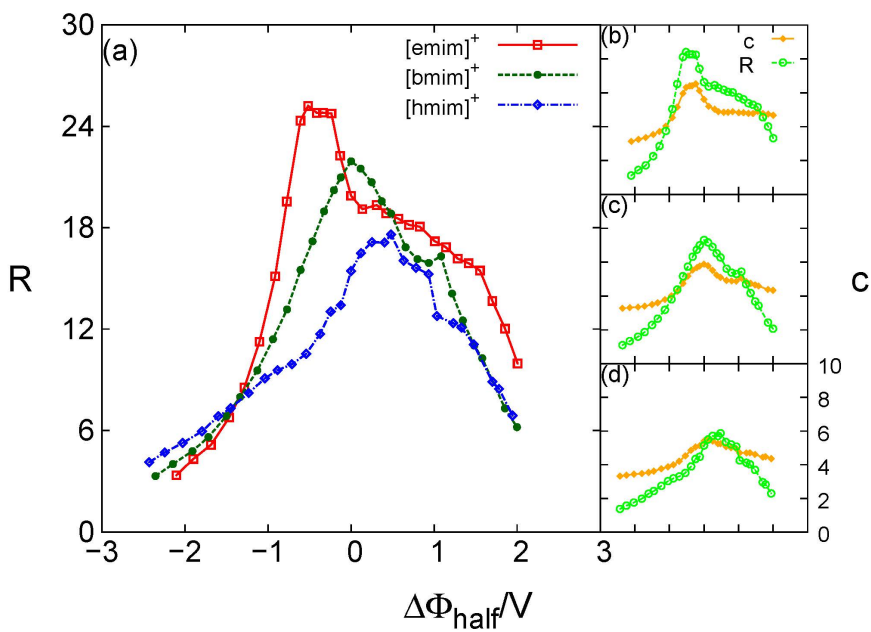


Figure 4.10: (a) Differential ion capacity R as a function of $\Delta\Phi_{\text{half}}$, obtained in three RTILs. Differential capacitance c and differential ion capacity R are compared for each system; (b) $[\text{emim}]^+\text{BF}_4^-$; (c) $[\text{bmim}]^+\text{BF}_4^-$; (d) $[\text{hmim}]^+\text{BF}_4^-$.

Despite some discrepancies above, however, we note the similarities between overall patterns of DC and DIC.

We then compare anodic and cathodic DIC. Overall behaviors are consistent with DC in that R is higher at positive potential. The cathodic R decreases faster and becomes lower than anodic counterpart as the potential is lowered further. With these consistencies between DC and DIC, we can draw more detailed picture of capacitive behaviors in our systems. Smaller BF_4^- anions accumulate near anode more effectively and thus shield more potential than the cations at cathode. Exceptional case is $[\text{emim}]^+$ cation at low negative potential, in that we can see from DIC curve that the cation is more sensitive to electrode potential at this range of voltage. A complete picture of ion accumulation would be more complex, not only due to ion size, but also other factors, such as ion shape, charge distribution, and orientation as well as specific interaction with electrode.^[66]

We compare R of all three systems in Figure 4.10 (a). DIC shows similar dependence on alkyl chain length with DC. First, the maximum R decreases with increasing alkyl chain length. Second, the potential of maximum DIC shifts to positive side: -0.24, 0 and 0.25 V for $[\text{emim}]^+\text{BF}_4^-$, $[\text{bmim}]^+\text{BF}_4^-$ and $[\text{hmim}]^+\text{BF}_4^-$, respectively. Reversed dependence on alkyl chain length at high negative potential is also observed in DIC.

Chapter 5

Conclusions

We explored interfacial structure and differential capacitance behavior of imidazolium-based RTILs with BF_4^- anion between two parallel graphene electrodes via MD simulations, and the dependence of alkyl chain length in cations were studied with $[\text{emim}]^+$, $[\text{bmim}]^+$, and $[\text{hmim}]^+$. Cations and anions in our RTILs make a layering structure over a wide range of electrode potential. Both imidazolium ring and alkyl chain of the cation in the first solvent layer have a tendency to be oriented parallel to the electrode surface and the extent of the latter becomes stronger with increase of their length. Differential capacitance curves in three RTILs were found to be bell-shaped decreasing with increase of the electrode potential. We found that $[\text{emim}]^+ \text{BF}_4^-$ makes distinctively higher cathodic capacitance in the range of low electrode potential, whereas anodic capacitance was higher for the most other cases in our RTILs due to screening efficiency by small anions.

We conclude by presenting a perspective on performance of the capacitors of our RTILs and our rationale for their different behavior in capacitance. It was presented in this part that differential capacitance decreases

with increasing the alkyl chain length over the wide range of the potential. The simulation results of our study, combined with previously reported experiment results, representing conductivity decreasing from $[\text{emim}]^+\text{BF}_4^-$ to $[\text{hmim}]^+\text{BF}_4^-$,^[67,68] suggests that the RTILs with shorter alkyl chain provides better performance as an electrolyte for EDLC. A plausible picture for different capacitance behaviors of the three RTILs was given in terms of liquid structure. We demonstrated that the ion accumulation in the nearest layer makes major contribution to some aspects of capacitance behavior, such as peaks of DC curves as well as their overall trends. The other aspects that the above scheme is inapplicable to may be subject to a potential screening by further layers of RTIL electrolyte. In the future study, it is worthwhile to examine capacitive responses of ionic layers further upon electric double layer and detailed molecular effects in them, paid attention to the effect of the alkyl chain.

Part II

Effects of Cyano-Group in Anion on Differential Capacitance and Charging Mechanism

Chapter 6

Introduction

Electric double layer capacitors (EDLCs) are promising devices used for energy storage due to their high capacitance, which can be achieved by a distinctive interfacial structure, electric double layer (EDL) formed at the electrode. Ions in electrolyte of EDLCs, where ionic liquids (ILs) as well as aqueous electrolytes are commonly used, in contrast to dielectric materials, screen the electrode charges completely at sub-nanometer length scale to form a prominent EDL, with which the electrode can store more charges^[1,69]. The structure of EDL thus crucially affects the capacitance, with a change of the stored charges in response to the external electric potential^[2,17,70].

Much research on EDLCs has been dedicated to understanding of the dependence of differential capacitance (DC) on electrode potential. To explain DC behaviors, different theoretical approaches have been made. Bell-shaped^[5-7,15-17] and camel-shaped^[5-14] curves are explained by a mean field theory with “lattice saturation effect”^[2-4,70] in which capacitance decreases as the electrode potential increases because electric double layer is thick-

ened. As ion concentration increases, two maxima in camel-shaped DC get closer and eventually merge into single maximum of bell-shaped curve which is located at potential of zero charge (PZC). Monte Carlo simulation studies provide an alternative explanation of camel-shaped DC based on a coarse-grained model of ILs with neutral chain^[6,18]. Neutral beads form “latent voids” near PZC. Maxima of DC at an intermediate potential are generated by replacement of “latent voids” by charged beads. In addition, the self-consistent mean field models explain the camel-shaped DC curve with the dependence of permittivity on the distance from the electrode surface^[5,8].

Experimental studies of EDLCs have reported varied shapes of DC curves, even for the cases with the same set of electrolyte and electrode material. For the imidazolium-based ionic liquids, the camel-shaped DC curves were observed at glassy carbon electrode^[10], but U-shaped curves were found in the case of glassy carbon^[37], highly oriented pyrolytic graphite (HOPG)^[38], and graphene electrodes^[71]. ILs with 1-ethyl-3-methylimidazolium cation with different anions show camel-shaped curves^[72]. On the other hand, bell-shaped^[15] and U-shaped^[73] curves were reported for 1-butyl-3-methylimidazolium tetrafluoroborate at the gold electrode.

To elucidate the microscopic picture of capacitance behavior of the system, both experimental^[74–77] and simulation^[7,30,40,78,79] studies have paid attention to charging mechanism of ions. Various mechanisms have been reported, namely anion-dominated^[30,77–79], cation-dominated^[30,40], counterion-dominated^[7], and equally-contributed^[74,75]. The charging mechanisms of the systems have even been found to be a function of electric potential^[7,30,40,76–79]. In spite of the great number of investigations of IL-electrode interfacial systems^[5–17,27–30,37,38,40,71,73–79], relation between charging mechanism and

differential capacitance is still unclear.

Ionic liquids are engineered ionic materials which stay in the liquid phase at ambient temperatures, and are commonly employed as electrolytes in EDLCs due to their high ion conductivity and electrochemical stability^[1,20,69,70]. Rather recently developed and alternative to conventional electrolytes, ILs have unique properties such as non-volatility, non-flammability, solubility of both polar and nonpolar solutes, and easy recycling. Another remarkable feature of ILs is their enormous diversity generated by combinations of different cations and anions^[20]. Often composed of organic ions, such combinations have been expanded by chemical tuning of ion structures^[80,81].

Among the variety of ILs, the cyano-based have unique properties and have attracted different kinds of applications. Some liquids were suggested as possible solvent material for extractive distillation due to their high selectivity and reasonable solubility such as tetracyanoborate($[B(CN)_4]^-$)-based ILs and 1-ethyl-3-methylimidazolium dicyanamide ($[emim]^+[N(CN)_2]^-$) for aromatic/nonaromatic and ethanol/water separation, respectively^[82]. 1-butyl-3-methylimidazolium thiocyanate ($[bmim]^+[SCN]^-$) and 1-butyl-3-methylimidazolium tricyanomethanide ($[bmim]^+[C(CN)_3]^-$) were used as extracting solvents as they have high solubility of carbohydrates and sugar alcohols^[83]. 1-ethyl-3-methylimidazolium thiocyanate ($[emim]^+[SCN]^-$) was employed as a local probe molecule in 2D-IR experiments because it does not affect structure and dynamics when it is mixed with other ILs^[84]. High solubility of carbon dioxide was utilized in CO₂ capturing^[85,86]. Dicyanamide($[N(CN)_2]^-$)-based ILs have low viscosity and were applied in electrodeposition of metals^[87]. Due to high conductivity and low viscosity, cyano-based ILs have

been widely applied in dye-sensitized solar cells^[88–90] as well as EDLCs^[91].

Understanding the charging mechanism is very important when one utilizes ILs as energy storage material for EDLCs. The charging mechanism has been examined by counting the number of ions in the pore of electrode materials^[40,74–77]. It was demonstrated that the effect of further ionic layers and the ion exchange behavior therein is required to be considered to explain the molecular origin of the DC behavior^[7,17]. One of the attempts was to evaluate the charge of ionic layers with fixed thickness out of a number of trials^[7]. The optimal thickness, however, was determined in an *ad hoc* manner, and little microscopic insight could be obtained from the result. To overcome this issue, we previously found in the Part I that the DC behavior can be explained with the interfacial layer in which ions are most actively accumulated. Nevertheless, it was not so straightforward to explain the saturation of DC at further potentials, which was predicted in mean field theory with “lattice saturation effect”^[2–4,70].

The purpose of the present part is to investigate charging mechanism of EDLC with ILs and its molecular origin by decomposing it into contribution of each ionic species. This part extends the previous part, where the cations were varied with different alkyl chain lengths, by systematically considering the effect of anions with charged functional groups. We examine the effect of cyano functional group of anion on electric double layer structure, differential capacitance and charging mechanism at graphene electrode, employing ILs with 1-ethyl-3-methylimidazolium ([emim]⁺) cation. Anions contain one to four cyano groups, which are thiocyanate ([SCN][−]), dicyanamide ([N(CN)₂][−]), tricyanomethanide ([C(CN)₃][−]), and tetracyanoborate ([B(CN)₄][−]), respectively.

The present part is organized as follows. Chapter 7 provides a brief description of the model system and simulation method. In Chapter 8, electric double layer structure, differential capacitance and charging mechanism of EDLC systems are analyzed to investigate their dependence on number of CN-groups. Conclusions are given in Chapter 9.

Chapter 7

Models and Methods

Four different cyano-based ILs are employed as dielectric material in this comparative study, namely 1-ethyl-3-methylimidazolium thiocyanate ($[\text{emim}]^+[\text{SCN}]^-$), 1-ethyl-3-methylimidazolium dicyanamide ($[\text{emim}]^+[\text{N}(\text{CN})_2]^-$), 1-ethyl-3-methylimidazolium tricyanomethanide ($[\text{emim}]^+[\text{C}(\text{CN})_3]^-$), and 1-ethyl-3-methylimidazolium tetracyanoborate ($[\text{emim}]^+[\text{B}(\text{CN})_4]^-$), respectively. A total of 1024 ion pairs are confined between basal plains of graphene electrodes for each system [Figure 7.1]. Each electrode consists of a rigid single graphene sheet of 1792 sp^2 -hybridized carbon atoms^[51], with dimensions $68.6 \times 67.9 \text{ \AA}^2$. We employed a Cartesian coordinate system where graphene electrodes spanned xy -plane and are located at $z = \pm z_0$. Electrode separation $d(= 2z_0)$ was determined by NPT ensemble simulation and fixed during NVT simulations. The respective values are 60.5, 65.3, 75.3 and 84.5 \AA for $[\text{emim}]^+[\text{SCN}]^-$, $[\text{emim}]^+[\text{N}(\text{CN})_2]^-$, $[\text{emim}]^+[\text{C}(\text{CN})_3]^-$ and $[\text{emim}]^+[\text{B}(\text{CN})_4]^-$. $[\text{emim}]^+$ cation was modeled with flexible all-atom force fields^[49,50]. Anion models are taken from previous study of bulk ILs^[92]. The parameters are compiled in supporting information of Ref50 and92. Total

electrode charge Q_e was varied from 0 to $\pm 34 e$ with an increment of $2 e$, which reproduced the same charge density increment as Part I.

GROMACS program was employed for the whole simulation process^[52]. The equation of motion was integrated using velocity Verlet algorithm with a time step of 1 fs. Coulomb interaction was computed by Particle Mesh Ewald Summation with correction for slab geometry^[53]. The vacuum regions are introduced under and over the capacitor such that the whole simulation cell spans $-3z_0 < z < 3z_0$. Five independent trajectories were sampled. We equilibrated the system for 25 ns with simulated annealing from 500K to 350K. 10 ns production runs were then conducted with Nosé-Hoover thermostat at 350K.

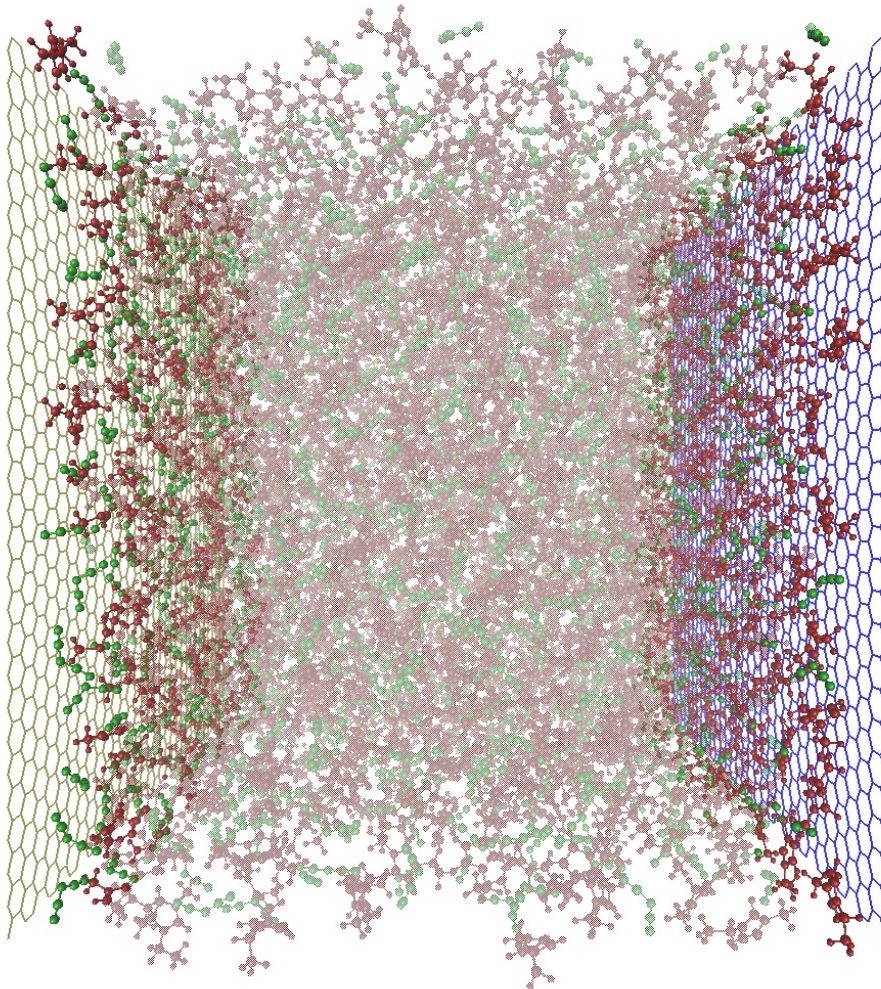


Figure 7.1: Representative snapshot of our systems. Blue: cathode with charge $Q_e = -32e$, Yellow: anode with the opposite charge, Red: $[\text{emim}]^+$ cations, Green: $[\text{N}(\text{CN})_2]^-$ anions, Highlighted: Ions in the interfacial layers. Counterions are attracted to and coions are expelled from the charged electrodes.

Chapter 8

Results and Discussion

8.1 Interfacial Structure

We first investigate the structure of ILs near graphene electrode. Number density distribution $n_\alpha(z)$ of the ionic species α is integrated from local, center of mass distribution of ions $n_\alpha(x', y', z)$,

$$n_\alpha(z) = A_0^{-1} \int_{-x_0}^{x_0} \int_{-y_0}^{y_0} dx' dy' n_\alpha(x', y', z); A_0 = 4x_0y_0 \quad (8.1)$$

with the electrode surface area A_0 . The average ion densities $n_\alpha(z)$ of four ILs are exhibited in Figure 8.1. Regardless of anion species and electrode charge, cations and anions form solvent layer within $\Delta z \leq 6$ Å from the graphene surface and show a significant oscillation behavior along z . This is consistent with previous studies, in which ionic layers are formed near flat surfaces^[7,9,17,23,25,26,33,34,54–56]. For the neutral charge cases in the bottom panels, the first solvation layers of [emim]⁺ are located at $\Delta z = 3.8$ Å. As more cyano groups are attached, the first solvation layer of anion is located closer to graphene sheet. The respective values are 3.6 Å for [SCN]⁻, 3.6

Å for $[\text{N}(\text{CN})_2]^-$ and 3.5 Å for $[\text{C}(\text{CN})_3]^-$. Bulky $[\text{B}(\text{CN})_4]^-$ anions with tetrahedral geometry make the solvation layer at further distance (4.3 Å) than other anions, even further than cation. Affinities to graphene surface of ions are in the following order: small, planar ($[\text{SCN}]^-$, $[\text{N}(\text{CN})_2]^-$, $[\text{C}(\text{CN})_3]^-$) > large, planar ($[\text{emim}]^+$) > large, spherical ($[\text{B}(\text{CN})_4]^-$) anions.

As the electrodes are more highly charged, the first solvent layer is filled with more counterions: the number density distribution becomes higher and narrower. Coions are gradually expelled from the charged electrode. Alternating layers of counterions and coions, namely electric double layers are eventually formed. In the cases of $[\text{C}(\text{CN})_3]^-$ and $[\text{B}(\text{CN})_4]^-$ (left, top panel of Figure 8.1 (c) and (d), respectively), anions make double-layered structure near highly charged anode. This is accompanied with change of packing structure of anions.

8.2 Electric Potentials and Differential Capacitances

Average charge density distribution $\rho_\alpha(z)$ is defined as

$$\rho_\alpha(z) = A_0^{-1} \int_{-x_0}^{x_0} \int_{-y_0}^{y_0} dx' dy' \rho_\alpha(x', y', z), \quad (8.2)$$

where $\rho_\alpha(x', y', z)$ is the local, atomic charge density of ionic species α . The results of four ILs are displayed in Figure 8.2. Ion charge densities oscillate near graphene surface and these behaviors diminish within 10 Å. This is consistent with previous studies of different ILs^[7,9,12–14,17,25,27,60,61]. The charge density oscillation of $[\text{B}(\text{CN})_4]^-$ extends further, up to 15 Å from the electrode. This is due to the symmetric structure in the anion which makes it harder to screen out partial charges.

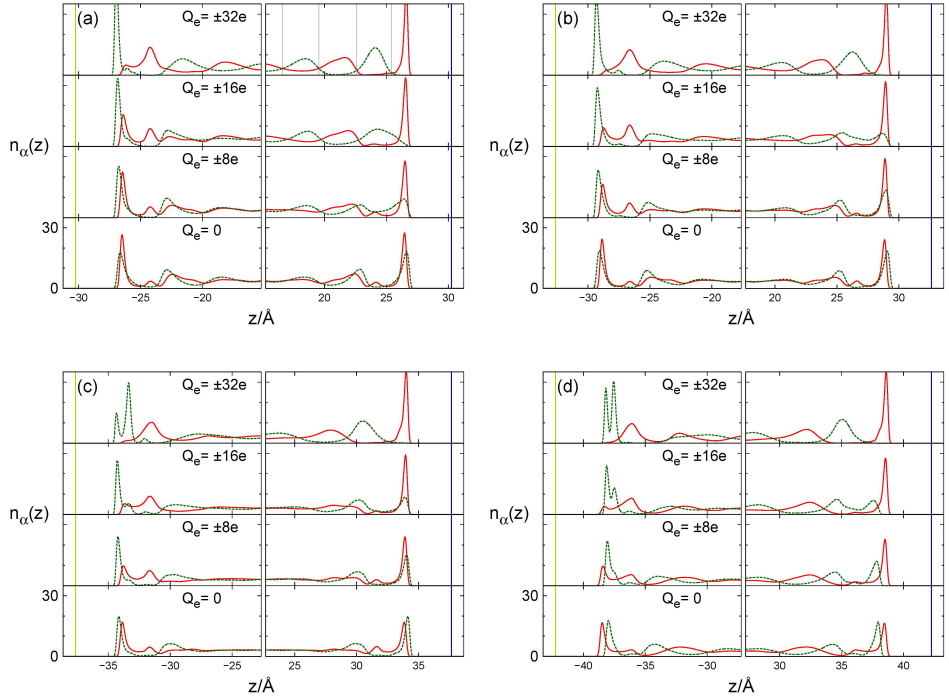


Figure 8.1: Number density distribution $n_\alpha(z)$ of the ions in four ionic liquids: (a) $[\text{emim}]^+[\text{SCN}]^-$, (b) $[\text{emim}]^+[\text{N}(\text{CN})_2]^-$, (c) $[\text{emim}]^+[\text{C}(\text{CN})_3]^-$, and (d) $[\text{emim}]^+[\text{B}(\text{CN})_4]^-$. The cation and anion number density distributions are represented by red and green curves, respectively. The locations of the electrode are indicated by yellow blue (anode) and blue (cathode) vertical lines. Black vertical lines are the borderlines between ionic layers. Counterions are abundant in the interfacial layer. Plots in the upper panels are the cases with the largest electrode charge Q_e .

The electric potential profile between two electrodes is calculated by Poisson equation:

$$\Phi_{\alpha}(z) = -4\pi \int_0^z dz(z - z')\rho_{\alpha}(z'), \quad (8.3)$$

where $\rho_{\alpha}(z')$ is the charge density from Eq. (8.2). Total electric potential profile which is summation of three components, $\Phi_{\text{total}}(z) = \Phi_{\text{cation}}(z) + \Phi_{\text{anion}}(z) + \Phi_{\text{electrode}}(z)$, are shown in Figure 8.3 for four liquids. The potentials of zero charge(PZC) between the electrode and the bulk region are found to be 0.26, 0.15, 0.09, and -0.01 V for $[\text{emim}]^+[\text{SCN}]^-$, $[\text{emim}]^+[\text{N}(\text{CN})_2]^-$, $[\text{emim}]^+[\text{C}(\text{CN})_3]^-$, and $[\text{emim}]^+[\text{B}(\text{CN})_4]^-$, respectively. This is in opposite trend with the affinity to graphene surface in a sense that ions with larger affinity are populated closer to the electrode. The partial charges of cation in Figure 8.2 are located closer than those of anion and positive PZCs are generated.

When the electrodes are charged, $\Phi_{\text{total}}(z)$ becomes nearly constant at $\Delta z \geq 20 \text{ \AA}$ after sharp drop at $\Delta z \leq 4 \text{ \AA}$. This is ascribed to ions forming electric double layer at $\Delta z \leq 20 \text{ \AA}$ and screening the electric field from charged electrode. We consider the whole system as a sequence of two half cells and divide $\Delta\Phi_{\text{tot}}$ between charged electrodes into cathodic and anodic potential:

$$\Delta\Phi_{\text{half}} = \Phi_{\text{electrode}} - \Phi_{\text{bulk}}, \quad (8.4)$$

$$\Delta\Phi_{\text{tot}} = \Delta\Phi_{\text{half}}^{(+)} - \Delta\Phi_{\text{half}}^{(-)}, \quad (8.5)$$

and $\Delta\Phi_{\text{half}}$ monotonically increases with electrode charge (see inset of Figure 8.4). We explore the differential behavior of electrode charge by evalu-

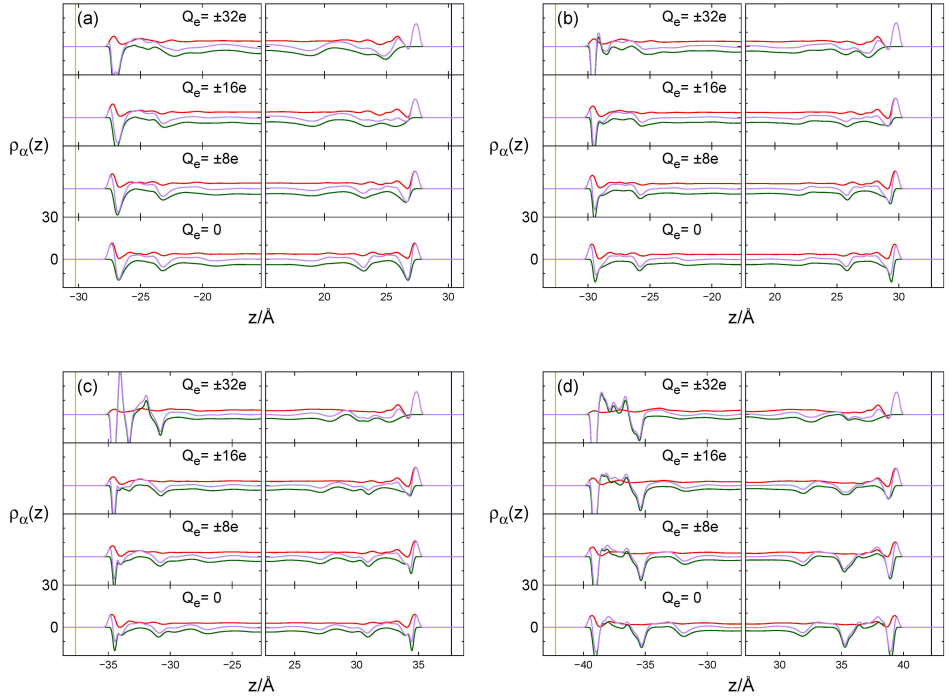


Figure 8.2: Charge density distribution $\rho_\alpha(z)$ of the ions in four ionic liquids: (a) $[\text{emim}]^+[\text{SCN}]^-$, (b) $[\text{emim}]^+[\text{N}(\text{CN})_2]^-$, (c) $[\text{emim}]^+[\text{C}(\text{CN})_3]^-$, (d) $[\text{emim}]^+[\text{B}(\text{CN})_4]^-$. The cation, anion and total charge density distributions are represented by red, green, and purple curves, respectively. Plots in the upper panels are the cases with the largest electrode charge Q_e .

ating the differential capacitance (DC),

$$c = \frac{\partial Q_e}{A_0 \partial \Delta \Phi_{\text{half}}}, \quad (8.6)$$

which is obtained by the same protocol as Part I: 29 windows of $Q_e - \Delta \Phi_{\text{half}}$ plot are fitted into parabolas and analytical derivatives are evaluated.

The DC curves for four systems are displayed in Figure 8.4. DC curves of all four liquids are characterized by the maximum at negative potential. The maximum values of capacitances are similar to each other. The maximum occurs at lower potential as the anion has more cyano groups: -0.82, -1.58 and -2.17 V for $[\text{emim}]^+[\text{SCN}]^-$, $[\text{emim}]^+[\text{N}(\text{CN})_2]^-$ and $[\text{emim}]^+[\text{C}(\text{CN})_3]^-$, respectively. The capacitances decrease at intermediate negative potential, just before the maximum peak. The respective regions are -0.15 to -0.41 V for $[\text{emim}]^+[\text{SCN}]^-$, 0.0 to -0.98 V for $[\text{emim}]^+[\text{N}(\text{CN})_2]^-$, -0.34 to -1.38 V for $[\text{emim}]^+[\text{C}(\text{CN})_3]^-$ and -0.7 to -1.18 V for $[\text{emim}]^+[\text{B}(\text{CN})_4]^-$. DC behaviors at positive potential are more complex. The capacitances are nearly unchanged near PZC. Such trends are extended to higher potentials for $[\text{SCN}]^-$ and $[\text{N}(\text{CN})_2]^-$ anions. On the other hand, $[\text{C}(\text{CN})_3]^-$ shows capacitance minimum at high positive potential, but maximum is observed for $[\text{B}(\text{CN})_4]^-$. DC behavior of $[\text{emim}]^+[\text{B}(\text{CN})_4]^-$ is consistent with an experimental study in that it exhibits a high capacitance at the negative potential^[93]. On the other hand, $[\text{emim}]^+[\text{N}(\text{CN})_2]^-$ shows a different trend from the camel-shaped curve at platinum electrode^[72]. However, a direct comparison between experiments and simulations is rather limited because the shape of DC curve could depend on several factors, namely electrolyte concentration^[72,94], chemical structure of ions^[33,95], ion clustering structure^[96], electrode material^[97,98], electrode topology^[12], and so on. Still, higher and

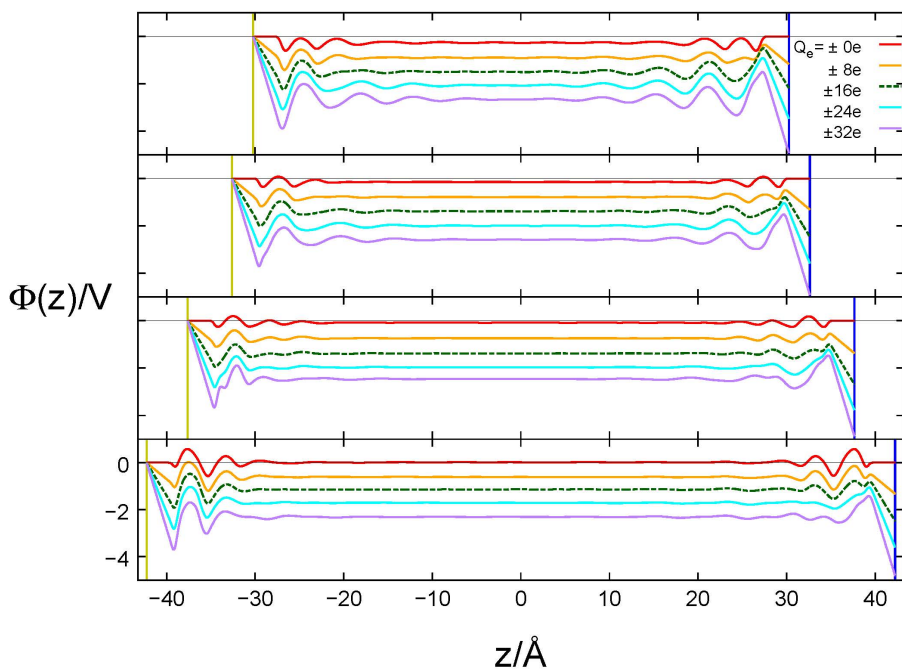


Figure 8.3: Electric potential $\Phi_{\text{total}}(z)$ in four ionic liquids. Top: $[\text{emim}]^+[\text{SCN}]^-$; second: $[\text{emim}]^+[\text{N}(\text{CN})_2]^-$; third: $[\text{emim}]^+[\text{C}(\text{CN})_3]^-$; bottom: $[\text{emim}]^+[\text{B}(\text{CN})_4]^-$. Blue: cathode, Yellow: anode.

narrower DC peaks at negative potentials are pronounced compared with other studies. Structural analysis of these peaks will be provided in following sections.

8.3 Ion Exchange in the Electric Double Layer

To understand the molecular origin of DC behaviors, a couple of simulation studies have examined the ion exchange behavior of ionic layers^[7,17]. One of the attempts was to evaluate the charge of ionic layers with fixed thickness. 10 Å, out of a number of trials, was reported to be the best thickness reproducing differential capacitance^[7]. However, this value may be argued to be too thin compared with the common thickness of electric double layers, 20 - 30 Å, inside which ionic layers, or oscillation of ionic charges, still remains. The optimal thickness was determined by an *ad hoc* manner, and little microscopic insight could be obtained from the result. On the other hand, we found in the previous part that the capacitance maximum occurs at the potential where ions are most actively accumulated in the interfacial layer^[17]. Nevertheless, “lattice saturation effect”^[2-4,70] was not reproduced in which DC is saturated at further potentials.

In the present section we systematically expand our scope to further ionic layers and investigate the ion exchange behavior between them. Starting from the interfacial layer, the alternating layers of cations and anions in Figure 8.1 are defined as *i*-th ionic layers one by one. The borderlines between the ionic layers are depicted in Figure 8.1 (a) and their definition is explained in Appendix B. We consider the number of ionic species α up

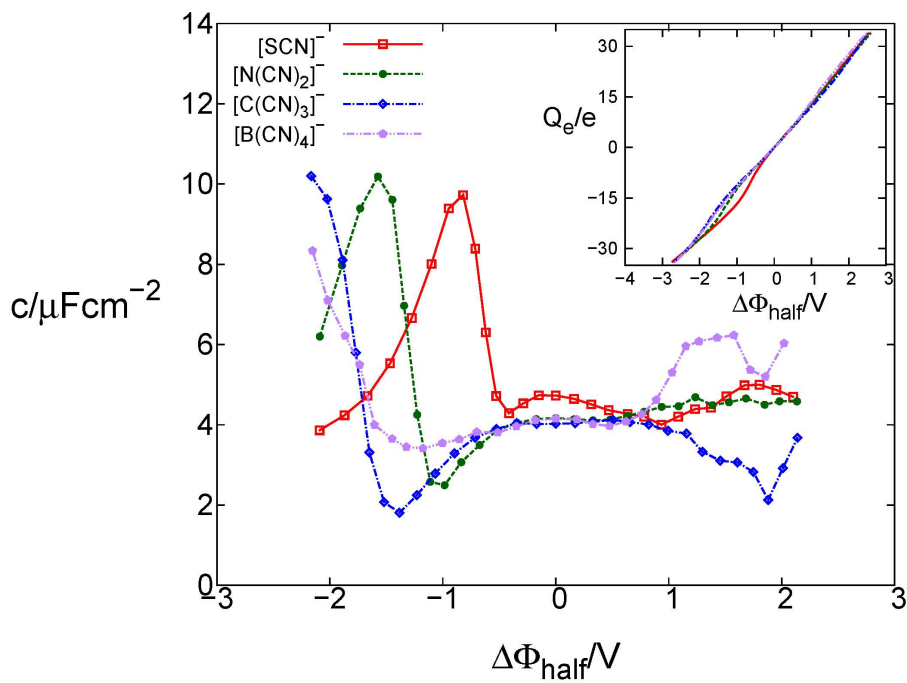


Figure 8.4: Electrode charge Q_e and differential capacitances c as a function of $\Delta\Phi_{\text{half}}$, obtained in $[\text{emim}]^+[\text{SCN}]^-$, $[\text{emim}]^+[\text{N}(\text{CN})_2]^-$, $[\text{emim}]^+[\text{C}(\text{CN})_3]^-$, and $[\text{emim}]^+[\text{B}(\text{CN})_4]^-$.

to i -th ionic layers N_α^i defined as

$$N_\alpha^i = A_0 \left| \int_{\text{electrode}}^{\textit{i-th layer}} dz' n_\alpha(z') \right|, \quad (8.7)$$

where $n_\alpha(z')$ is the number density from Eq. (8.1). The complementary charge of ionic layers, Q^i , is then calculated,

$$Q^i = -(q_{\text{an}} N_{\text{an}}^i + q_{\text{cat}} N_{\text{cat}}^i), \quad (8.8)$$

where the negative sign is introduced to set Q^i to be comparable to the electrode charge, Q_e . Q^i increases when anions are adsorbed in or cations are desorbed from the ionic layers, and shows monotonic increase with electric potential as well as Q_e does^[17].

We define differential capacitance of ionic layers (DCIL) as

$$c^i = \frac{\partial Q^i}{A_0 \partial \Delta \Phi_{\text{half}}}, \quad (8.9)$$

and c^i , with $i = 1, 3$, and 5 are evaluated and compared with DC in Figure 8.5. c^1 shows maximum at negative potential. The maximum location and peak width show coincidence with DC, consistently with Part I. Decreases in capacitance at intermediate negative potential are also observed in DCIL curves. c^1 has much larger value than DC. This is ascribed to over-screening behavior of ions in which excess charges are accumulated in the first layer and compensated by alternating layers^[17,65]. As more ionic layers are considered, DCIL becomes more similar to DC. This discloses that DC behavior is mainly generated by ion exchange between electric double layer and bulk region.

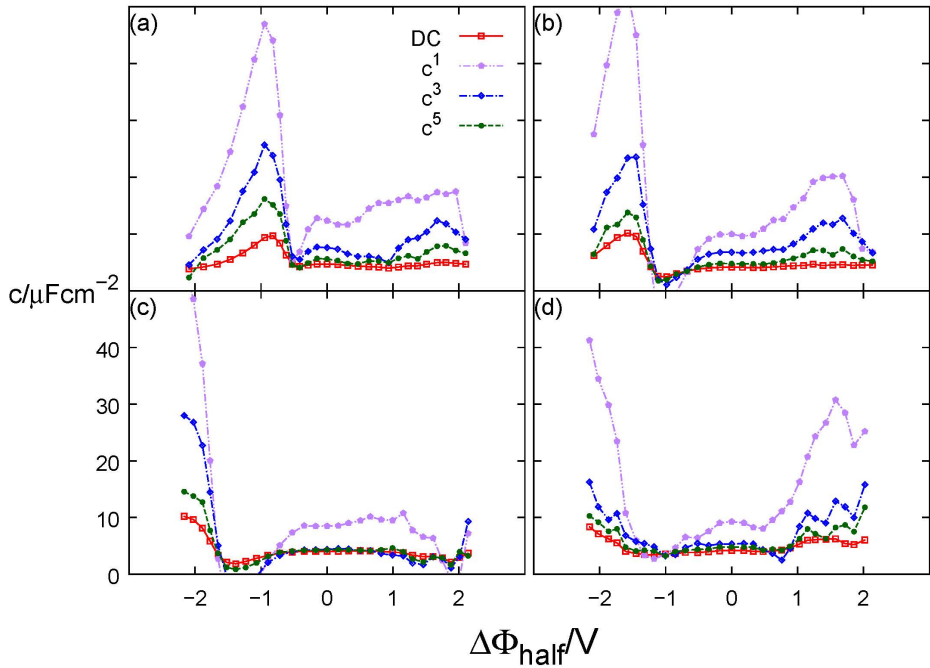


Figure 8.5: Differential capacitances c and differential capacitance of ionic layers (DCIL) c^1 , c^3 , and c^5 as a function of $\Delta\Phi_{\text{half}}$ in four ionic liquids: (a) $[\text{emim}]^+[\text{SCN}]^-$; (b) $[\text{emim}]^+[\text{N}(\text{CN})_2]^-$; (c) $[\text{emim}]^+[\text{C}(\text{CN})_3]^-$; (d) $[\text{emim}]^+[\text{B}(\text{CN})_4]^-$.

8.4 Differential Charging Mechanism

Experimental studies examined the charging mechanism of the system by counting the number of ions in the pore of electrode materials^[74-77], and a simulation study found a correlation between DC and the total number of ions in the pore^[40]. The effect of further ionic layers, however, is proposed to be considered to explain the whole DC behavior as demonstrated in the previous part and Section 8.3, thus we explore the charging mechanism of EDLCs with such consideration.

Defined from the number of ions, DCIL can be interpreted as the differential charging mechanism of ions. We decompose DCIL into cation and anion contributions. The charge and DCIL component of ionic species α are defined similarly to eqs (8.8) and (8.9) as

$$Q_{\alpha}^i = -q_{\alpha}N_{\alpha}^i, \quad (8.10)$$

and

$$c_{\alpha}^i = \frac{\partial Q_{\alpha}^i}{A_0 \partial \Delta \Phi_{\text{half}}}, \quad (8.11)$$

and both cation and anion components are functions of electric potential. DCIL c^5 is decomposed into contributions by cation and anion, and compared with DC in Figure 8.6. The positive value of DCIL components means that the corresponding ions behave as expected near a charged electrode: counterions are attracted to and coions are expelled from the electrode. DCIL behaviors of four liquids are mainly governed by respective anion behaviors in that anion contribution is larger than cation one and shows similar trend with DC. The high peak of DCIL c_{an}^5 at negative potential means that anions(coions) are rapidly desorbed from the ionic layers near

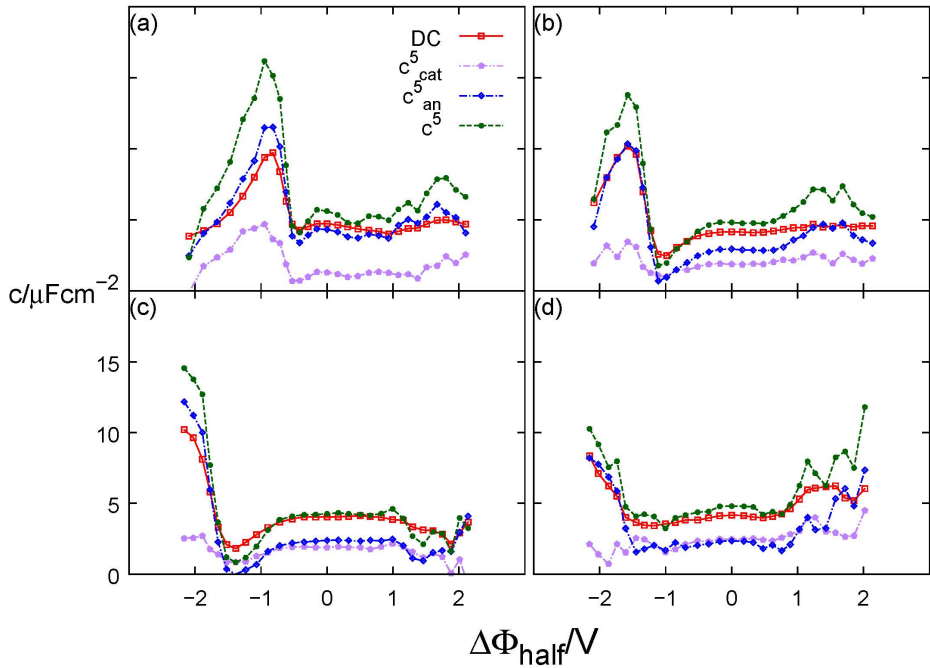


Figure 8.6: Differential capacitances c , differential capacitance of ionic layers (DCIL) c^5 , and its divided components: c_{an}^5 and c_{cat}^5 as a function of $\Delta\Phi_{\text{half}}$ in four ionic liquids: (a) $[\text{emim}]^+[\text{SCN}]^-$; (b) $[\text{emim}]^+[\text{N}(\text{CN})_2]^-$; (c) $[\text{emim}]^+[\text{C}(\text{CN})_3]^-$; (d) $[\text{emim}]^+[\text{B}(\text{CN})_4]^-$.

the cathode. We interpret the differential charging mechanism of the system with this insight. Both anion and cation contribute to DCIL behaviors around PZC. The anion desorption is suppressed at intermediate negative potential where both DC and DCIL decrease. As the potential is further lowered, the anions are rapidly desorbed and maximum peak is formed.

To further elucidate the anion desorption mechanism, the number density distributions of different potential regions are compared each other. First, three potential regions of different DC behaviors are defined: the starting point of cathode charging, DC maximum and DC minimum, respectively. They are numbered in DC curve at Figure 8.7 (a). The number density distribution of ions in three potential regions are displayed in Figure 8.7 (b)-(d). At the starting point of cathode charging [Figure 8.7 (b)], both cations and anions are found in the first ionic layer. As the cathode is charged, anion peak at $26.3 < z < 27.0 \text{ \AA}$ become smaller: anions are expelled from this region. However, anions are accumulated in the intermediate region at $25.4 < z < 26.3 \text{ \AA}$, which is still in the first layer so that the number of anion decreases gradually. On the other hand, the potential region 4-6 [Figure 8.7 (c)] is the DC maximum region. The anion peak at Figure 8.7 (b) is already disappeared. As the cathode is more negatively charged, the anion distribution in the first layer decreases, whereas that in the second layer increases. The anions in the first layer are expelled to the second layer and the number of anion rapidly decreases. At the potential region 7-9 [Figure 8.7 (d)] DC is decreased. The decrease in the number of anion is suppressed because most of anions are already expelled from the first layer and only few anions dwell in the first layer.

The potential of rapid anion desorption is lowered as the anion size is

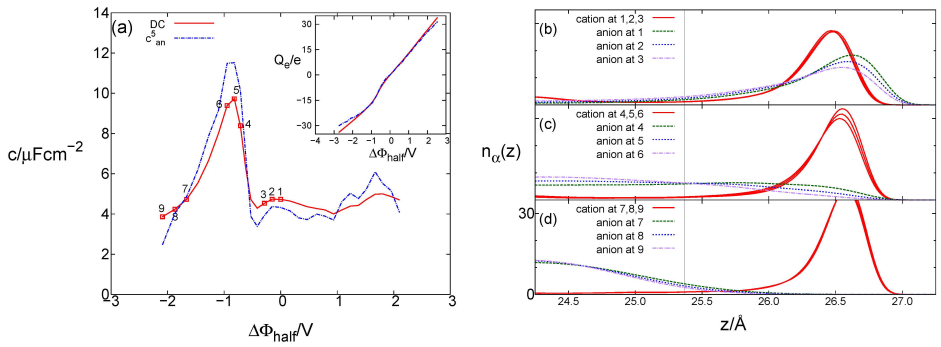


Figure 8.7: (a): Electrode charge Q_e and differential capacitances c as a function of $\Delta\Phi_{\text{half}}$, obtained in $[\text{emim}]^+[\text{SCN}]^-$. Q_e is compared with charge of ionic layers Q_{an}^5 and c is compared with differential capacitance of ionic layers c_{an}^5 , respectively. Maximum and minimum points of DC at negative potential are numbered. (b)-(d): Number density distribution $n_\alpha(z)$ of the ions near the cathode obtained in $[\text{emim}]^+[\text{SCN}]^-$. Black vertical line is the borderline between first and second ionic layers of which definition is explained in Supporting Information. As the cathode is more negatively charged, anions(coion) are expelled from the first ionic layer.

increased. Stronger repulsive force from cathode is required for larger anion to be desorbed from electric double layer. In the case of $[\text{emim}]^+[\text{C}(\text{CN})_3]^-$, suppression of cation desorption is responsible for capacitance minimum at high positive potential. On the other hand, DCIL of $[\text{emim}]^+[\text{B}(\text{CN})_4]^-$ shows different trend from the capacitance maximum at high positive potential. DCIL keeps increasing as the potential is increased because the anions are more actively adsorbed in the electric double layer. This discrepancy may be subject to the exchange of partial charges exerted by orientational rearrangement of the ions, which is averaged out in DCIL as it is defined from the center of mass distribution of the ions.

As a quantitative analysis of relative contribution, the fraction of anion component x_{an} is calculated for each case and displayed in Figure 8.8:

$$x_{\text{an}} = \frac{c_{\text{an}}^5}{c^5}. \quad (8.12)$$

At the potential region near PZC, x_{an} remain nearly unchanged because both components are stationary in those potential regions : 77, 60, 55, and 48 % for $[\text{emim}]^+[\text{SCN}]^-$, $[\text{emim}]^+[\text{N}(\text{CN})_2]^-$, $[\text{emim}]^+[\text{C}(\text{CN})_3]^-$ and $[\text{emim}]^+[\text{B}(\text{CN})_4]^-$, respectively. This decrease of anion component is ascribed to anion size in that larger anions are harder to rearrange in response to electric potential. However, $[\text{emim}]^+$ cations are exchanged more actively and the DC in Figure 8.4 are comparable to each other. As the potential is lowered, x_{an} decreases at intermediate potential and increases at further potential. This is the same behavior with c_{an}^5 in Figure 8.6. Exceptional case is $[\text{emim}]^+[\text{SCN}]^-$. Both c_{an}^5 and c_{cat}^5 increase and x_{an} decreases in the DC peak region. There are two points where x_{an} exceeds 100 %: high negative potential for $[\text{emim}]^+[\text{SCN}]^-$ and high positive potential for $[\text{emim}]^+[\text{C}(\text{CN})_3]^-$.

Excess charges are exchanged by anion desorption/adsorption and compensated by cation desorption/adsorption, which is the opposite behavior to what is expected near negative/positive electrode, respectively.

It is noteworthy that the $[\text{emim}]^+[\text{SCN}]^-$ case is anion-dominant in charging mechanism in overall potential range. $[\text{emim}]^+[\text{BF}_4]^-$ has also been investigated to show anion-dominant mechanism due to size disparity in ionic species as smaller anion responds more actively to the electrode potential^[17]. It describes very well the phenomena in our study, especially near 0 V, where the contribution of anion becomes greater in ILs with the smaller anion. Since there is no significant interaction between the electrolyte molecules and the electrodes, the size-disparity is assumed to be the most possible consideration. It is, therefore, very interesting that the x_{an} near the peak of DC varies extremely with different ILs. We close our discussion by speculating that a collective behavior in ionic structure may cause this abrupt change in the trend of charging mechanism.

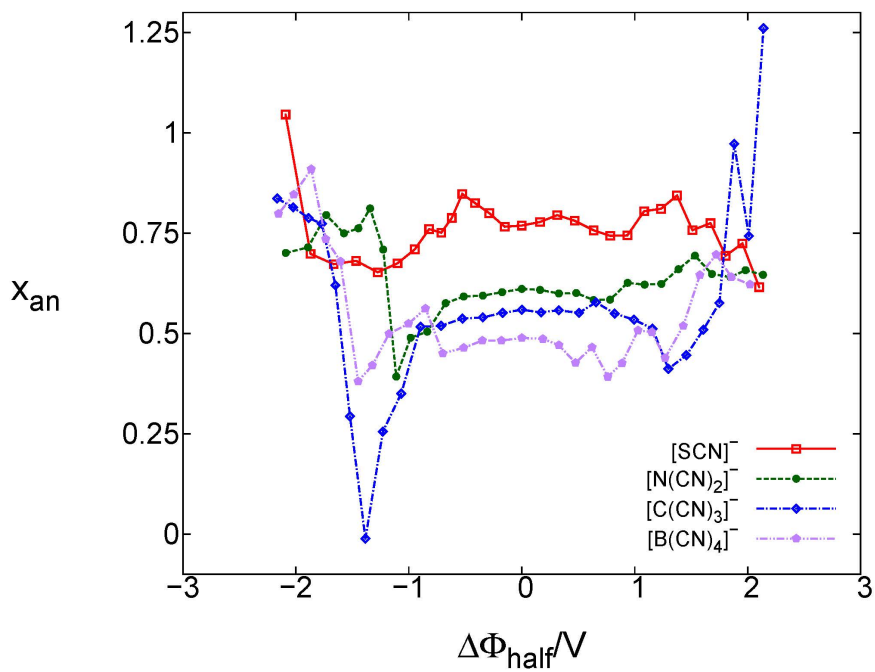


Figure 8.8: Fraction of anion component x_{an} as a function of $\Delta\Phi_{\text{half}}$, obtained in $[\text{emim}]^+[\text{SCN}]^-$, $[\text{emim}]^+[\text{N}(\text{CN})_2]^-$, $[\text{emim}]^+[\text{C}(\text{CN})_3]^-$, and $[\text{emim}]^+[\text{B}(\text{CN})_4]^-$ at 350K.

Chapter 9

Conclusions

Electric double layer structure and differential capacitance behavior of cyano-based ionic liquids with $[\text{emim}]^+$ cation near graphene electrode were explored by MD simulations. The dependence on the number of cyano groups in anions was investigated with $[\text{SCN}]^-$, $[\text{N}(\text{CN})_2]^-$, $[\text{C}(\text{CN})_3]^-$ and $[\text{B}(\text{CN})_4]^-$. Cations and anions in our ionic liquids make alternating layers near charged electrode. Differential capacitance curves of four ionic liquids were found to have the maximum at negative potential. The maximum capacitances were similar to each other, but the peak location shifted to further potential as the number of cyano groups is increased. Combined with previous experimental studies representing that $[\text{emim}]^+[\text{SCN}]^-$ has the widest electrochemical window^[91,99], our simulation results suggest that EDLC with $[\text{SCN}]^-$ provides best performance among the cyano-based anions.

We conclude by presenting our rationale for capacitance behaviors of four ionic liquids in terms of liquid structure. We systematically extended our consideration of layering structures from the interfacial layer to further layers and examined the ion exchange between them. The ion exchange be-

tween electric double layer and bulk region turned out to be the main factor generating DC behaviors. The differential charging mechanism of ions are investigated by decomposing the ion exchange behavior into cation and anion contributions. The charging mechanism, as well as electric double layer structure and differential capacitance was found to be a function of electric potential. The capacitance maxima of all liquids at negative potential are generated by rapid desorption of respective anions. $[\text{emim}]^+[\text{SCN}]^-$, is an exceptional case in that both cation and anion are responsible for the capacitance maximum. The exchange of partial charge as well as ion exchange in the ionic layers can affect the DC behaviors. The present part provides a molecular insight to electrochemical application of ionic liquids in which ions form layered structure near the electrode. In the future study, it is worthwhile to examine the detailed molecular effect of ion structure in capacitive behaviors, paid attention to the charging mechanism.

Chapter 10

Effects of Alkyl Chain Length in Cation on Charging Mechanism

In this additional chapter, alkylimidazolium ionic liquids in part I, 1-C_n(n=2,4,6)-3-methylimidazolium tetrafluoroborate are revisited. We investigate how differential capacitance and differential charging mechanism are affected by alkyl chain length of imidazolium cation. The number density distribution in Figure 4.1 is analyzed with the same protocol as presented in Section 8.3 and 8.4.

10.1 Ion Exchange in the Electric Double Layer

First, ionic layers are introduced as explained in Appendix B: interfacial layer is the first layer and alternating layers of cations and anions are consecutively defined as i -th layers. The number of ionic species α up to i -th layers N_{α}^i is counted

$$N_{\alpha}^i = A_0 \left| \int_{\text{electrode}}^{\textit{i-th layer}} dz' n_{\alpha}(z') \right|, \quad (10.1)$$

where $n_\alpha(z')$ is the number density from Eq. (4.1). The complementary charge of ionic layers, Q^i , is then calculated,

$$Q^i = -(q_{\text{an}}N_{\text{an}}^i + q_{\text{cat}}N_{\text{cat}}^i), \quad (10.2)$$

where the negative sign is introduced to set Q^i to increase with electric potential as well as Q_e does^[17].

The differential capacitance of ionic layers (DCIL)

$$c^i = \frac{\partial Q^i}{A_0 \partial \Delta \Phi_{\text{half}}}, \quad (10.3)$$

with $i = 1, 3$, and 5 are evaluated and compared with DC in Figure 10.1. The maximum location and peak width of c^1 coincide with those of DC, consistently with Section 4.3 and 8.3. c^1 is much larger than DC due to overscreening behavior^[17,65]: excess charges are accumulated in the first layer. As we expand the consideration into further layers, alternating layers compensate the excess charges and DCIL shows more similar value to DC. This is consistent with Section 8.3 and supports our idea that DC behavior mainly stems from the ion exchange between electric double layer and bulk region.

10.2 Differential Charging Mechanism

The differential charging mechanism of ions is investigated by decomposing DCIL into cation and anion contributions. The complementary charge of ionic layers, Q^i , is divided into charge component of ionic species α

$$Q_\alpha^i = -q_\alpha N_\alpha^i, \quad (10.4)$$

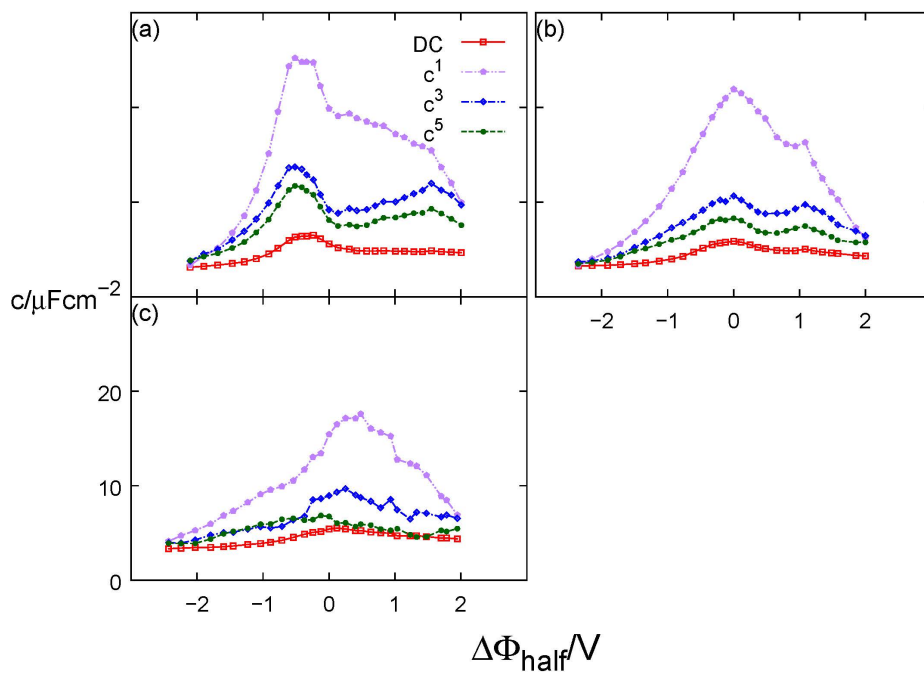


Figure 10.1: Differential capacitances c and differential capacitance of ionic layers (DCIL) c^1 , c^3 , and c^5 as a function of $\Delta\Phi_{\text{half}}$ in three ionic liquids: (a) $[\text{emim}]^+\text{BF}_4^-$; (b) $[\text{bmim}]^+\text{BF}_4^-$; (c) $[\text{hmim}]^+\text{BF}_4^-$.

and the DCIL component is evaluated.

$$c_{\alpha}^i = \frac{\partial Q_{\alpha}^i}{A_0 \partial \Delta \Phi_{\text{half}}}, \quad (10.5)$$

DCIL c^5 and its components c_{cat}^5 , c_{an}^5 are compared with DC in Figure 10.2. DC behaviors of three systems are mainly governed by anion exchange behavior. The anion component shows similar trend with DC and is larger than cation one in the whole potential region. The DCIL maxima are mainly originated from rapid anion exchange. However, both cation and anion are responsible for DC peak at negative potential for [emim]⁺ system. As the alkyl chain of cation is lengthened, both cation and anion exchange are suppressed in wide potential region. This is ascribed to steric effect exerted by charge neutral functional group. On the other hand, reversed dependence of capacitance on alkyl chain length at high negative potential ($\Delta \Phi_{\text{half}} < -1.3$ V) is also observed in the anion contribution.

As we demonstrated that DC peak stems from the rapid exchange of the anions, the final question to complete mechanistic explanation of DC behaviors in our systems would be “what makes such a rapid exchange of anions in DC peak region?”. This is not so straightforward to answer because the rapid exchange is made by collective motion of ions in that both cations and anions are exchanged simultaneously. We further speculate that anion-dominated charging mechanisms of our systems are due to small anion sizes in that the exchange of anions is made more easily than that of cations in broad potential region. More detailed simulation studies are worthy of performing in the near future.

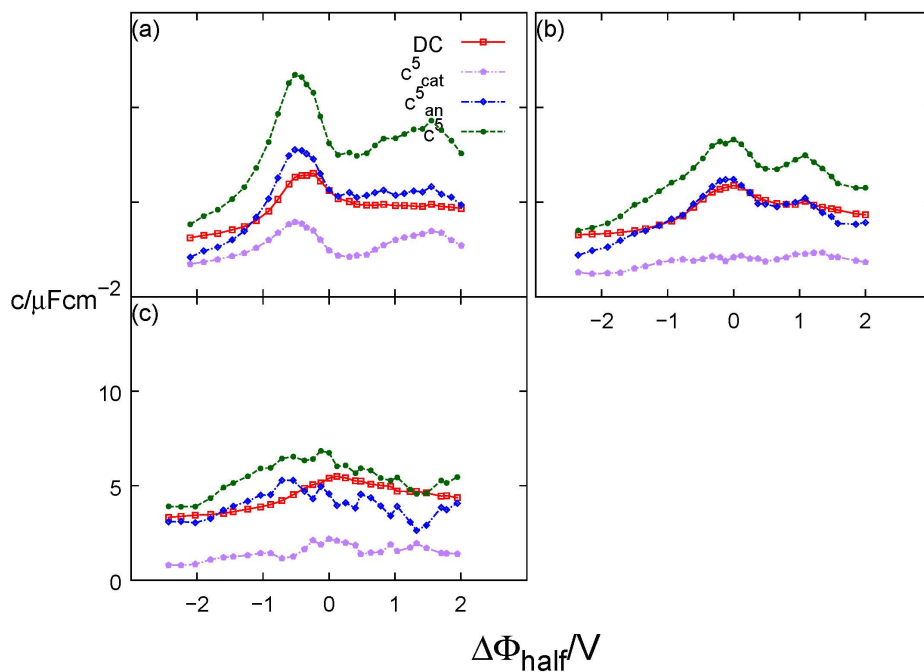


Figure 10.2: Differential capacitances c , differential capacitance of ionic layers(DCIL) c^5 , and its divided components: c^5_{an} and c^5_{cat} as a function of $\Delta\Phi_{\text{half}}$ in three ionic liquids: (a) $[\text{emim}]^+\text{BF}_4^-$; (b) $[\text{bmim}]^+\text{BF}_4^-$; (c) $[\text{hmim}]^+\text{BF}_4^-$.

Appendix

Appendix A

Ion Number Difference and its Derivative

We first define ion number N_α as the number of ion species α in the nearest layer. Then number difference ΔN is defined as $N_{\text{anion}} - N_{\text{cation}}$ so that its value increases from negative to positive with electrode potential: there are more cations near cathode (negative potential) and vice versa. The ion population at the first layer is different with the sign of electrode charge: the first layer of cathode is cation-abundant and the opposite holds for anode.

At the neutral electrode, however, it is ambiguous to define the first layer between two possible options, one definition making the layer cation-abundant and the other anion-abundant. Because the sign of the electrode charge is zero, we are free to consider it as the cathode or the anode. We thus regard the neutral electrodes as infinitesimally charged ones: the anode with charge $+\varepsilon$ and the cathode with $-\varepsilon$, respectively, and then the former becomes anion-abundant and the latter cation-abundant.

The derivative of ΔN with respect to $\Delta\Phi_{\text{half}}$ is then evaluated with the same protocol as is DC, subtracting ΔN at a negatively/positively charged

electrode from its value at the neutral cathode/anode, respectively.

$$\delta\Delta N(Q_e < 0) = \Delta N(Q_e < 0) - \Delta N(Q_e = -\varepsilon) \quad (\text{A.1})$$

$$\delta\Delta N(Q_e > 0) = \Delta N(Q_e > 0) - \Delta N(Q_e = +\varepsilon) \quad (\text{A.2})$$

Now, we can make smooth differentiation of $\delta\Delta N$ because it has unique value (= 0) at zero potential.

Appendix B

Transition from specific ionic layers to electric double layers

We defined the crossing points of cation and anion distributions as the borderlines between ionic layers as depicted in Figure 8.1. (a). The thicknesses of ionic layers are displayed in Figure B.1.

Ions near neutral electrode make layering structure due to specific interaction between graphene surface and the ions. (bottom panels of Figure 8.1.) As the electrodes are more highly charged, counterions are attracted to and coions are expelled from the electrode. In this process some specific layers disappear and the thicknesses show sharp transition at intermediate potentials. Alternating layers of counterions and coions, electric double layers are eventually formed. We selected the converged values at high potentials as the thicknesses of ionic layers in the electric double layer, evaluating the charge of ionic layers Q^i .

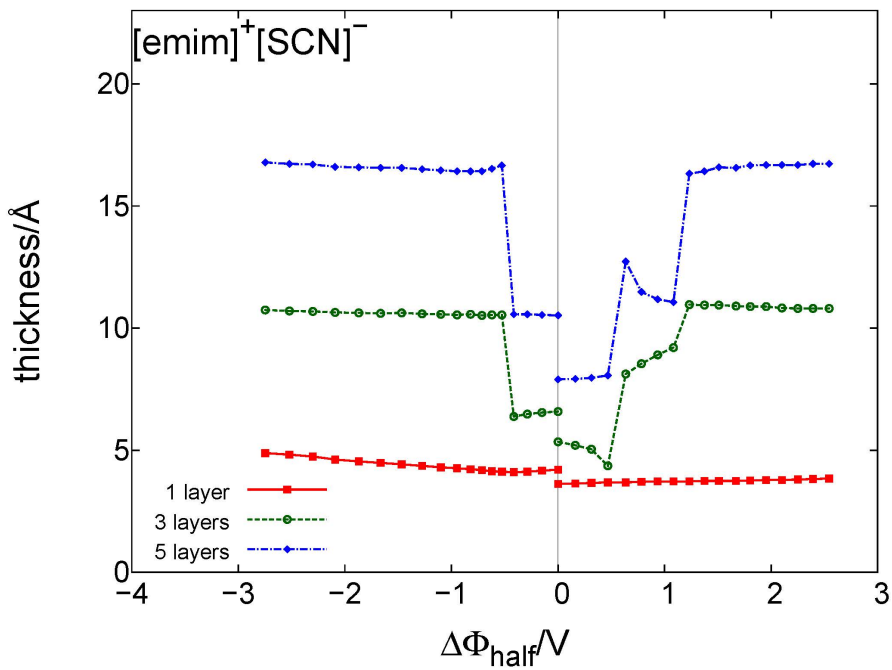


Figure B.1: Thicknesses of ionic layers as a function of $\Delta\Phi_{\text{half}}$, obtained in $[\text{emim}]^+[\text{SCN}]^-$.

Bibliography

- [1] González, A.; Goikolea, E.; Barrena, J. A.; Mysyk, R. Review on supercapacitors: Technologies and materials. *Renewable and Sustainable Energy Reviews* **2016**, *58*, 1189.
- [2] Kornyshev, A. A. Double-layer in ionic liquids: paradigm change? *The journal of physical chemistry. B* **2007**, *111*, 5545–5557.
- [3] Borukhov, I.; Andelman, D.; Orland, H. Steric Effects in Electrolytes: A Modified Poisson-Boltzmann Equation. *Physical review letters* **1997**, *79*, 435.
- [4] Goodwin, Z. A.; Feng, G.; Kornyshev, A. A. Mean-Field Theory of Electrical Double Layer In Ionic Liquids with Account of Short-Range Correlations. *Electrochimica Acta* **2017**, *225*, 190.
- [5] Lauw, Y.; Horne, M. D.; Rodopoulos, T.; Leermakers, F. A. M. Room-temperature ionic liquids: excluded volume and ion polarizability effects in the electrical double-layer structure and capacitance. *Physical review letters* **2009**, *103*, 117801.
- [6] Trulsson, M.; Algotsson, J.; Forsman, J.; Woodward, C. E. Differential

- Capacitance of Room Temperature Ionic Liquids: The Role of Dispersion Forces. *The Journal of Physical Chemistry Letters* **2010**, *1*, 1191.
- [7] Hu, Z.; Vatamanu, J.; Borodin, O.; Bedrov, D. A comparative study of alkylimidazolium room temperature ionic liquids with FSI and TFSI anions near charged electrodes. *Electrochimica Acta* **2014**, *145*, 40.
- [8] Lauw, Y.; Horne, M. D.; Rodopoulos, T.; Nelson, A.; Leermakers, F. A. M. Electrical double-layer capacitance in room temperature ionic liquids: ion-size and specific adsorption effects. *The journal of physical chemistry. B* **2010**, *114*, 11149–11154.
- [9] Vatamanu, J.; Borodin, O.; Smith, G. D. Molecular insights into the potential and temperature dependences of the differential capacitance of a room-temperature ionic liquid at graphite electrodes. *Journal of the American Chemical Society* **2010**, *132*, 14825–14833.
- [10] Lockett, V.; Horne, M.; Sedev, R.; Rodopoulos, T.; Ralston, J. Differential capacitance of the double layer at the electrode/ionic liquids interface. *Physical chemistry chemical physics : PCCP* **2010**, *12*, 12499–12512.
- [11] Costa, R.; Pereira, C. M.; Silva, F. Double layer in room temperature ionic liquids: influence of temperature and ionic size on the differential capacitance and electrocapillary curves. *Physical chemistry chemical physics : PCCP* **2010**, *12*, 11125–11132.
- [12] Vatamanu, J.; Cao, L.; Borodin, O.; Bedrov, D.; Smith, G. D. On the Influence of Surface Topography on the Electric Double Layer Structure

- and Differential Capacitance of Graphite/Ionic Liquid Interfaces. *The Journal of Physical Chemistry Letters* **2011**, *2*, 2267.
- [13] Vatamanu, J.; Borodin, O.; Smith, G. D. Molecular simulations of the electric double layer structure, differential capacitance, and charging kinetics for N-methyl-N-propylpyrrolidinium bis(fluorosulfonyl)imide at graphite electrodes. *The Journal of Physical Chemistry B* **2011**, *115*, 3073–3084.
- [14] Vatamanu, J.; Borodin, O.; Bedrov, D.; Smith, G. D. Molecular Dynamics Simulation Study of the Interfacial Structure and Differential Capacitance of Alkylimidazolium Bis(trifluoromethanesulfonyl)imide [Cnmim][TFSI] Ionic Liquids at Graphite Electrodes. *The Journal of Physical Chemistry C* **2012**, *116*, 7940.
- [15] Su, Y.-Z.; Fu, Y.-C.; Yan, J.-W.; Chen, Z.-B.; Mao, B.-W. Double layer of Au(100)/ionic liquid interface and its stability in imidazolium-based ionic liquids. *Angewandte Chemie (International ed. in English)* **2009**, *48*, 5250–5253.
- [16] Alam, M. T.; Masud, J.; Islam, M. M.; Okajima, T.; Ohsaka, T. Differential Capacitance at Au(111) in 1-Alkyl-3-methylimidazolium Tetrafluoroborate Based Room-Temperature Ionic Liquids. *The Journal of Physical Chemistry C* **2011**, *115*, 19797.
- [17] Jo, S.; Park, S.-W.; Shim, Y.; Jung, Y. Effects of Alkyl Chain Length on Interfacial Structure and Differential Capacitance in Graphene Supercapacitors: A Molecular Dynamics Simulation Study. *Electrochimica Acta* **2017**, *247*, 634.

- [18] Georgi, N.; Kornyshev, A. A.; Fedorov, M. V. The anatomy of the double layer and capacitance in ionic liquids with anisotropic ions: Electrostriction vs. lattice saturation. *Journal of Electroanalytical Chemistry* **2010**, *649*, 261.
- [19] Armand, M.; Endres, F.; MacFarlane, D. R.; Ohno, H.; Scrosati, B. Ionic-liquid materials for the electrochemical challenges of the future. *Nature materials* **2009**, *8*, 621–629.
- [20] Kirchner, B., Ed. *Ionic Liquids*; Topics in Current Chemistry; Springer, 2010; Vol. 290.
- [21] Endres, F.; MacFarlane, D.; Abbott, A. *Electrodeposition from Ionic Liquids*; John Wiley & Sons, 2008.
- [22] Dou, Q.; Sha, M. L.; Fu, H. Y.; Wu, G. Z. Molecular dynamics simulation of the interfacial structure of [Cnmim][PF₆] adsorbed on a graphite surface: effects of temperature and alkyl chain length. *Journal of Physics: Condensed Matter* **2011**, *23*, 175001.
- [23] Feng, G.; Zhang, J. S.; Qiao, R. Microstructure and Capacitance of the Electrical Double Layers at the Interface of Ionic Liquids and Planar Electrodes. *The Journal of Physical Chemistry C* **2009**, *113*, 4549–4559.
- [24] Shim, Y.; Kim, H. J. Nanoporous carbon supercapacitors in an ionic liquid: a computer simulation study. *ACS nano* **2010**, *4*, 2345–2355.
- [25] Feng, G.; Qiao, R.; Huang, J.; Dai, S.; Sumpter, B. G.; Meunier, V. The importance of ion size and electrode curvature on electrical double

- layers in ionic liquids. *Physical chemistry chemical physics : PCCP* **2010**, *13*, 1152–1161.
- [26] Merlet, C.; Salanne, M.; Rotenberg, B.; Madden, P. A. Imidazolium Ionic Liquid Interfaces with Vapor and Graphite: Interfacial Tension and Capacitance from Coarse-Grained Molecular Simulations. *The Journal of Physical Chemistry C* **2011**, *115*, 16613–16618.
- [27] Shim, Y.; Jung, Y.; Kim, H. J. Graphene-Based Supercapacitors: A Computer Simulation Study. *The Journal of Physical Chemistry C* **2011**, *115*, 23574.
- [28] Shim, Y.; Kim, H. J.; Jung, Y. Graphene-based supercapacitors in the parallel-plate electrode configuration: Ionic liquids versus organic electrolytes. *Faraday Discuss.* **2012**, *154*, 249.
- [29] DeYoung, A. D.; Park, S.-W.; Dhumal, N. R.; Shim, Y.; Jung, Y.; Kim, H. J. Graphene Oxide Supercapacitors: A Computer Simulation Study. *The Journal of Physical Chemistry C* **2014**, *118*, 18472.
- [30] Park, S.-W.; DeYoung, A. D.; Dhumal, N. R.; Shim, Y.; Kim, H. J.; Jung, Y. Computer Simulation Study of Graphene Oxide Supercapacitors: Charge Screening Mechanism. *The journal of physical chemistry letters* **2016**, *7*, 1180–1186.
- [31] Dyatkin, B.; Zhang, Y.; Mamontov, E.; Kolesnikov, A. I.; Cheng, Y.; Meyer, H. M.; Cummings, P. T.; Gogotsi, Y. Influence of Surface Oxidation on Ion Dynamics and Capacitance in Porous and Nonporous Carbon Electrodes. *The Journal of Physical Chemistry C* **2016**, *120*, 8730.

- [32] Xu, K.; Ji, X.; Chen, C.; Wan, H.; Miao, L.; Jiang, J. Electrochemical double layer near polar reduced graphene oxide electrode: Insights from molecular dynamic study. *Elsevier* **2015**,
- [33] Liu, X.; Wang, Y.; Li, S.; Yan, T. Effects of anion on the electric double layer of imidazolium-based ionic liquids on graphite electrode by molecular dynamics simulation. *Electrochimica Acta* **2015**, *184*, 164–170.
- [34] Merlet, C.; Salanne, M.; Rotenberg, B.; Madden, P. A. Influence of solvation on the structural and capacitive properties of electrical double layer capacitors. *Electrochimica Acta* **2013**, *101*, 262–271.
- [35] Yu, Z.; Tetard, L.; Zhai, L.; Thomas, J. Supercapacitor electrode materials: nanostructures from 0 to 3 dimensions. *Energy & Environmental Science* **2015**, *8*, 702.
- [36] Hughes, Z. E.; Walsh, T. R. Computational chemistry for graphene-based energy applications: progress and challenges. *Nanoscale* **2015**, *7*, 6883–6908.
- [37] Alam, M. T.; Islam, M. M.; Okajima, T.; Ohsaka, T. Capacitance Measurements in a Series of Room-Temperature Ionic Liquids at Glassy Carbon and Gold Electrode Interfaces. *The Journal of Physical Chemistry C* **2008**, *112*, 16600.
- [38] Islam, M. M.; Alam, M. T.; Okajima, T.; Ohsaka, T. Electrical Double Layer Structure in Ionic Liquids: An Understanding of the Unusual Capacitance–Potential Curve at a Nonmetallic Electrode. *The Journal of Physical Chemistry C* **2009**, *113*, 3386.

- [39] Nagy, T.; Henderson, D.; Boda, D. Simulation of an electrical double layer model with a low dielectric layer between the electrode and the electrolyte. *The journal of physical chemistry. B* **2011**, *115*, 11409–11419.
- [40] Xing, L.; Vatamanu, J.; Borodin, O.; Bedrov, D. On the Atomistic Nature of Capacitance Enhancement Generated by Ionic Liquid Electrolyte Confined in Subnanometer Pores. *The journal of physical chemistry letters* **2012**, *4*, 132–140.
- [41] Xing, L.; Vatamanu, J.; Smith, G. D.; Bedrov, D. Nanopatterning of Electrode Surfaces as a Potential Route to Improve the Energy Density of Electric Double-Layer Capacitors: Insight from Molecular Simulations. *The journal of physical chemistry letters* **2012**, *3*, 1124–1129.
- [42] Li, S.; Feng, G.; Fulvio, P. F.; Hillesheim, P. C.; Liao, C.; Dai, S.; Cummings, P. T. Molecular Dynamics Simulation Study of the Capacitive Performance of a Binary Mixture of Ionic Liquids near an Onion-like Carbon Electrode. *The journal of physical chemistry letters* **2012**, *3*, 2465–2469.
- [43] Hu, Z.; Vatamanu, J.; Borodin, O.; Bedrov, D. A molecular dynamics simulation study of the electric double layer and capacitance of [BMIM][PF 6] and [BMIM][BF 4] room temperature ionic liquids near charged surfaces. *Physical Chemistry Chemical Physics* **2013**, *15*, 14234.
- [44] Vatamanu, J.; Xing, L.; Li, W.; Bedrov, D. Influence of temperature on

- the capacitance of ionic liquid electrolytes on charged surfaces. *Physical Chemistry Chemical Physics* **2014**, *16*, 5174–5182.
- [45] Vatamanu, J.; Vatamanu, M.; Borodin, O.; Bedrov, D. A comparative study of room temperature ionic liquids and their organic solvent mixtures near charged electrodes. *Journal of Physics: Condensed Matter* **2016**, *28*, 464002.
- [46] Klomfar, J.; Součková, M.; Pátek, J. Buoyancy density measurements for 1-alkyl-3-methylimidazolium based ionic liquids with tetrafluoroborate anion. *fluid phase equilibria* **2009**, *282*, 31.
- [47] Soriano, A. N.; Doma, B. T.; Li, M.-H. Measurements of the density and refractive index for 1-n-butyl-3-methylimidazolium-based ionic liquids. *The Journal of Chemical Thermodynamics* **2009**, *41*, 301.
- [48] Safarov, J.; Hassel, E. Thermodynamic properties of 1-hexyl-3-methylimidazolium tetrafluoroborate. *Journal of Molecular Liquids* **2010**, *153*, 153.
- [49] Lopes, J. N. C.; Deschamps, J.; Pádua, A. A. H. Modeling Ionic Liquids Using a Systematic All-Atom Force Field. *The Journal of Physical Chemistry B* **2004**, *108*, 2038.
- [50] Lopes, J. N. C.; Deschamps, J.; Pádua, A. A. H. Modeling Ionic Liquids Using a Systematic All-Atom Force Field. *The Journal of Physical Chemistry B* **2004**, *108*, 11250.
- [51] Hummer, G.; Rasaiah, J. C.; Noworyta, J. P. Water conduction through

- the hydrophobic channel of a carbon nanotube. *Nature* **2001**, *414*, 188–190.
- [52] Lindahl, E.; Hess, B.; van der Spoel, D. GROMACS 3.0: a package for molecular simulation and trajectory analysis. *Journal Of Molecular Modeling* **2001**, *7*, 306–317.
- [53] Yeh, I.-C.; Berkowitz, M. L. Ewald summation for systems with slab geometry. *The Journal of chemical physics* **1999**, *111*, 3155.
- [54] Li, H.; Endres, F.; Atkin, R. Effect of alkyl chain length and anion species on the interfacial nanostructure of ionic liquids at the Au(111)-ionic liquid interface as a function of potential. *Physical chemistry chemical physics : PCCP* **2013**, *15*, 14624–14633.
- [55] Li, H.; Wood, R. J.; Endres, F.; Atkin, R. Influence of alkyl chain length and anion species on ionic liquid structure at the graphite interface as a function of applied potential. *Journal of Physics: Condensed Matter* **2014**, *26*, 284115.
- [56] Li, M.-G.; Chen, L.; Zhong, Y.-X.; Chen, Z.-B.; Yan, J.-W.; Mao, B.-W. The electrochemical interface of Ag(111) in 1-ethyl-3-methylimidazolium bis(trifluoromethylsulfonyl)imide ionic liquid-A combined in-situ scanning probe microscopy and impedance study. *Electrochimica Acta* **2016**, *197*, 282–289.
- [57] Mahurin, S. M.; Surwade, S. P.; Crespo, M.; Dai, S. Probing the interaction of ionic liquids with graphene using surface-enhanced Raman spectroscopy. *Journal of Raman Spectroscopy* **2016**, *47*, 585.

- [58] Li, M.; Westover, A. S.; Carter, R.; Oakes, L.; Muralidharan, N.; Boire, T. C.; Sung, H.-J.; Pint, C. L. Noncovalent Pi-Pi Stacking at the Carbon-Electrolyte Interface: Controlling the Voltage Window of Electrochemical Supercapacitors. *ACS applied materials & interfaces* **2016**, *8*, 19558–19566.
- [59] Wen, R.; Rahn, B.; Magnussen, O. M. In Situ Video-STM Study of Adlayer Structure and Surface Dynamics at the Ionic Liquid/Au (111) Interface. *The Journal of Physical Chemistry C* **2016**, *120*, 15765.
- [60] Vatamanu, J.; Borodin, O.; Smith, G. D. Molecular Dynamics Simulation Studies of the Structure of a Mixed Carbonate/LiPF₆ Electrolyte near Graphite Surface as a Function of Electrode Potential. *The Journal of Physical Chemistry C* **2012**, *116*, 1114–1121.
- [61] Tazi, S.; Salanne, M.; Simon, C.; Turq, P.; Pounds, M.; Madden, P. A. Potential-induced ordering transition of the adsorbed layer at the ionic liquid/electrified metal interface. *The journal of physical chemistry. B* **2010**, *114*, 8453–8459.
- [62] Jeong, D.; Shim, Y.; Choi, M. Y.; Kim, H. J. Effects of solute electronic polarizability on solvation in a room-temperature ionic liquid. *The journal of physical chemistry. B* **2007**, *111*, 4920–4925.
- [63] Rotenberg, B.; Salanne, M. Structural Transitions at Ionic Liquid Interfaces. *The journal of physical chemistry letters* **2015**, *6*, 4978–4985.
- [64] Alam, M. T.; Islam, M. M.; Okajima, T.; Ohsaka, T. Measurements of Differential Capacitance at Mercury/Room-Temperature Ionic Liquids Interfaces. *The Journal of Physical Chemistry C* **2007**, *111*, 18326.

- [65] Bazant, M. Z.; Storey, B. D.; Kornyshev, A. A. Double layer in ionic liquids: overscreening versus crowding. *Physical review letters* **2011**, *106*, 046102.
- [66] Forse, A. C.; Merlet, C.; Griffin, J. M.; Grey, C. P. New Perspectives on the Charging Mechanisms of Supercapacitors. *Journal of the American Chemical Society* **2016**, *138*, 5731–5744.
- [67] Nishida, T.; Tashiro, Y.; Yamamoto, M. Physical and electrochemical properties of 1-alkyl-3-methylimidazolium tetrafluoroborate for electrolyte. *Journal of Fluorine Chemistry* **2003**, *120*, 135.
- [68] Stoppa, A.; Zech, O.; Kunz, W.; Buchner, R. The Conductivity of Imidazolium-Based Ionic Liquids from (−35 to 195) °C. A. Variation of Cation’s Alkyl Chain†. *Journal of Chemical & Engineering Data* **2009**, *55*, 1768.
- [69] Wang, G.; Zhang, L.; Zhang, J. A review of electrode materials for electrochemical supercapacitors. *Chemical Society reviews* **2011**, *41*, 797–828.
- [70] Fedorov, M. V.; Kornyshev, A. A. Ionic liquids at electrified interfaces. *Chemical reviews* **2014**, *114*, 2978–3036.
- [71] Oll, O.; Romann, T.; Siimenson, C.; Lust, E. Influence of chemical composition of electrode material on the differential capacitance characteristics of the ionic liquid | electrode interface. *Electrochemistry Communications* **2017**, *82*, 39.

- [72] Jitvisate, M.; Seddon, J. R. T. Direct Measurement of the Differential Capacitance of Solvent-Free and Dilute Ionic Liquids. *The journal of physical chemistry letters* **2017**, *9*, 126–131.
- [73] Lucio, A. J.; Shaw, S. K.; Zhang, J.; Bond, A. M. Large-Amplitude Fourier-Transformed AC Voltammetric Study of the Capacitive Electrochemical Behavior of the 1-Butyl-3-methylimidazolium Tetrafluoroborate–Polycrystalline Gold Electrode Interface. *The Journal of Physical Chemistry C* **2017**, *121*, 12136.
- [74] Prehal, C.; Weingarth, D.; Perre, E.; Lechner, R. T.; Amenitsch, H.; Paris, O.; Presser, V. Tracking the structural arrangement of ions in carbon supercapacitor nanopores using in situ small-angle X-ray scattering. *Energy & Environmental Science* **2015**, *8*, 1725.
- [75] Deschamps, M.; Gilbert, E.; Azais, P.; Raymundo-Piñero, E.; Ammar, M. R.; Simon, P.; Massiot, D.; Béguin, F. Exploring electrolyte organization in supercapacitor electrodes with solid-state NMR. *Nature materials* **2013**, *12*, 351–358.
- [76] Griffin, J. M.; Forse, A. C.; Tsai, W.-Y.; Taberna, P.-L.; Simon, P.; Grey, C. P. In situ NMR and electrochemical quartz crystal microbalance techniques reveal the structure of the electrical double layer in supercapacitors. *Nature materials* **2015**, *14*, 812–819.
- [77] Forse, A. C.; Griffin, J. M.; Merlet, C.; Bayley, P. M.; Wang, H.; Simon, P.; Grey, C. P. NMR Study of Ion Dynamics and Charge Storage in Ionic Liquid Supercapacitors. *Journal of the American Chemical Society* **2015**, *137*, 7231–7242.

- [78] Merlet, C.; Rotenberg, B.; Madden, P. A.; Taberna, P.-L.; Simon, P.; Gogotsi, Y.; Salanne, M. On the molecular origin of supercapacitance in nanoporous carbon electrodes. *Nature materials* **2012**, *11*, 306–310.
- [79] Merlet, C.; Péan, C.; Rotenberg, B.; Madden, P. A.; Daffos, B.; Taberna, P. L.; Simon, P.; Salanne, M. Highly confined ions store charge more efficiently in supercapacitors. *Nature communications* **2013**, *4*, 2701.
- [80] Marsh, K. N.; Boxall, J. A.; Lichtenthaler, R. Room temperature ionic liquids and their mixtures—a review. *Fluid Phase Equilibria* **2004**, *219*, 93–98.
- [81] Castner, E. W.; Wishart, J. F. Spotlight on ionic liquids. *The Journal of chemical physics* **2010**, *132*, 120901.
- [82] Gutiérrez, J. P.; Meindersma, G. W.; de Haan, A. B. COSMO-RS-Based Ionic-Liquid Selection for Extractive Distillation Processes. *Industrial & Engineering Chemistry Research* **2012**, *51*, 11518.
- [83] Conceição, L. J. A.; Bogel-Lukasik, E.; Bogel-Lukasik, R. A new outlook on solubility of carbohydrates and sugar alcohols in ionic liquids. *RSC Advances* **2012**, *2*, 1846.
- [84] Ren, Z.; Brinzer, T.; Dutta, S.; Garrett-Roe, S. Thiocyanate as a local probe of ultrafast structure and dynamics in imidazolium-based ionic liquids: water-induced heterogeneity and cation-induced ion pairing. *The journal of physical chemistry. B* **2015**, *119*, 4699–4712.

- [85] Kim, J. E.; Kim, H. J.; Lim, J. S. Solubility of CO₂ in ionic liquids containing cyanide anions: [c2mim][SCN], [c2mim][N(CN)₂], [c2mim][C(CN)₃]. *Fluid Phase Equilibria* **2014**, *367*, 151.
- [86] Babarao, R.; Dai, S.; Jiang, D.-e. Understanding the high solubility of CO₂ in an ionic liquid with the tetracyanoborate anion. *The journal of physical chemistry. B* **2011**, *115*, 9789–9794.
- [87] Deng, M.-J.; Chen, P.-Y.; Leong, T.-I.; Sun, I.-W.; Chang, J.-K.; Tsai, W.-T. Dicyanamide anion based ionic liquids for electrodeposition of metals. *Electrochemistry Communications* **2008**, *10*, 213.
- [88] Zhou, D.; Bai, Y.; Zhang, J.; Cai, N.; Su, M.; Wang, Y.; Zhang, M.; Wang, P. Anion Effects in Organic Dye-Sensitized Mesoscopic Solar Cells with Ionic Liquid Electrolytes: Tetracyanoborate vs Dicyanamide. *The Journal of Physical Chemistry C* **2010**, *115*, 816.
- [89] Zhang, M.; Zhang, J.; Bai, Y.; Wang, Y.; Su, M.; Wang, P. Anion-correlated conduction band edge shifts and charge transfer kinetics in dye-sensitized solar cells with ionic liquid electrolytes. *Physical chemistry chemical physics : PCCP* **2010**, *13*, 3788–3794.
- [90] Bai, Y.; Zhang, J.; Wang, Y.; Zhang, M.; Wang, P. Lithium-modulated conduction band edge shifts and charge-transfer dynamics in dye-sensitized solar cells based on a dicyanamide ionic liquid. *Langmuir : the ACS journal of surfaces and colloids* **2011**, *27*, 4749–4755.
- [91] Sun, G.-h.; Li, K.-x.; Sun, C.-g. Application of 1-ethyl-3-methylimidazolium thiocyanate to the electrolyte of electrochemical

- double layer capacitors. *Journal of Power Sources* **2006**, *162*, 1444–1450.
- [92] Dhungana, K. B.; Dhungana, K. B.; Faria, L. F. O.; Faria, L. F. O.; Wu, B.; Wu, B.; Liang, M.; Liang, M.; Ribeiro, M. C. C.; Ribeiro, M. C. C.; Margulis, C. J.; Margulis, C. J.; Castner, E. W. Structure of cyano-anion ionic liquids: X-ray scattering and simulations. *The Journal of chemical physics* **2016**, *145*, 024503.
- [93] Thiemann, S.; Sachnov, S.; Porscha, S.; Wasserscheid, P.; Zaumseil, J. Ionic Liquids for Electrolyte-Gating of ZnO Field-Effect Transistors. *The Journal of Physical Chemistry C* **2012**, *116*, 13536.
- [94] Zhang, Q.; Liu, X.; Yin, L.; Chen, P.; Wang, Y.; Yan, T. Electrochemical impedance spectroscopy on the capacitance of ionic liquid–acetonitrile electrolytes. *Electrochimica Acta* **2018**, *270*, 352.
- [95] Zheng, Y.; Engineering, C. o. C.; Environmental,; Anyang Institute of Technology,; 455000, A.; Henan,; China, P. R. Electrical Double Layer in Imidazolium Chloroaluminate Ionic Liquids and Its Influence on the Surface Morphology of Aluminium Deposits. *International Journal of Electrochemical Science* **2016**, 9585.
- [96] Ma, K.; Forsman, J.; Woodward, C. E. A Classical Density Functional Study of Clustering in Ionic Liquids at Electrified Interfaces. *The Journal of Physical Chemistry C* **2017**, *121*, 1742.
- [97] Müller, C.; Németh, K.; Vesztergom, S.; Pajkossy, T.; Jacob, T. The interface between HOPG and 1-butyl-3-methyl-imidazolium hexafluorophosphate. *Physical Chemistry Chemical Physics* **2015**, *18*, 916–925.

- [98] Costa, R.; Pereira, C. M.; Silva, A. F. Charge Storage on Ionic Liquid Electric Double Layer: The Role of the Electrode Material. *Electrochimica Acta* **2015**, *167*, 421.
- [99] Weingarh, D.; Czekaj, I.; Fei, Z.; Foelske-Schmitz, A.; Dyson, P. J.; Wokaun, A.; Koetz, R. Electrochemical Stability of Imidazolium Based Ionic Liquids Containing Cyano Groups in the Anion: A Cyclic Voltammetry, XPS and DFT Study. *Journal of the Electrochemical Society* **2012**, *159*, H611–H615.

국문초록

전기이중층 축전기는 높은 전기용량으로 인해 에너지 저장장치로서 주목받고 있다. 전기이중층 축전기의 미분 전기용량은 전압에 따라 바뀌는데 이는 전기이중층 구조가 변화하기 때문이다. 이 논문에서는 미분 전기용량의 거동이 전해질의 화학구조에 어떻게 영향을 받는지 분자동역학 시뮬레이션을 통해 연구하였다.

첫번째 파트에서는 양이온에 붙어있는 알킬사슬의 길이가 표면 구조와 전기적 성질에 어떤 영향을 주는지 알아보았다. 전해질로는 같은 음이온 테트라플로로보레이트와 세가지 다른 양이온, 1-에틸-3-메틸이미다졸륨, 1-뷰틸-3-메틸이미다졸륨, 1-헥실-3-메틸이미다졸륨을 각각 조합한 상온 이온성 액체를 채택하였다. 두 평행한 전극 사이에서 양이온들과 음이온들이 이온층을 형성하는 것을 확인하였다. 전극 표면의 양이온들은 주로 전극에 평행하게 분포해 있는 것을 보았다. 양이온의 이미다졸륨 고리가 그래핀과 파이-스태킹 구조를 형성하고, 알킬사슬이 전극에 평행하게 정렬되는 모습을 확인하였다. 세가지 액체의 미분 전기용량 모두 전압의 절대값이 증가함에 따라 감소하는 것을 발견하였다. 이온의 크기와 정렬 양상은 이온층 구조와 전기용량의 거동 모두에 영향을 준다. 양이온의 평행한 정렬은 알킬사슬이 길어질 수록 강화되는 것을 확인하였다. 미분 전기용량은 넓은 전압 영역에서 알킬사슬이 길어짐에 따라 감소하는 경향을 보인다. 이는 이온의 크기가 커져 입체장애가 강화되

이온 재배치가 방해되기 때문이다. 또한 크기가 작은 음이온이 재배치를 더 잘하기 때문에 양극 전기용량이 음극 전기용량보다 큰 것을 확인할 수 있었다. 전극 전하량과 전극 표면의 이온 개수를 전압에 대한 변화 양상의 측면에서 비교함으로써, 표면 이온층이 전기용량 거동에 주된 역할을 한다는 사실을 밝혀냈다.

두번째 파트에서는 싸이아노 작용기를 갖는 음이온의 구조가 전기이중층 구조와 전기적 성질에 어떤 영향을 주는지 알아보았다. 전해질로는 같은 양이온 1-에틸-3-메틸이미다졸륨 과 네가지 다른 음이온, 싸이오싸이아네이트, 다이싸이안아마이드, 트라이싸이아노메타나이드, 테트라싸이아노보레이트 을 각각 조합한 상온 이온성 액체를 채택하였다. 전하를 띤 전극 근처에서 양이온과 음이온들이 번갈아 분포하는 모습을 보였다. 네가지 시스템의 미분 전기용량이 음의 전압에서 최대값을 갖는 것을 확인하였다. 최대값은 서로 비슷하지만 최대값을 내는 전압은 음이온에 붙은 싸이아노 작용기의 개수가 늘어날 수록 더 음의 값으로 치우치는 현상을 보였다. 표면 이온층에서 시작해 점점 더 멀리 있는 이온층이 미분 전기용량에 미치는 영향을 체계적으로 조사하였다. 전극 전하량과 이온층의 전하량을 비교함으로써, 미분 전기용량의 거동이 전기이중층과 액체 구간 사이의 이온 교환에 의해 발생한다는 사실을 밝혀냈다. 이온 교환 거동을 양이온 성분과 음이온 성분으로 나누어 조사하였다. 그 결과 미분 충전 메커니즘이 전압에 강하게 의존한다는 사실과 네가지 시스템의 전기용량 최대값은 각각의 음이온이 전기이중층으로부터 빠르게 떨어져 나가는 전압구간에서 생겨난다는 사실을 밝혀냈다.

주요어: 전기이중층 축전기, 상온 이온성 액체, 그래핀 전극, 알킬이미다졸륨, 미분 전기용량, 표면 구조, 전기이중층 구조, 충전 메커니즘, 분자동역학 시뮬레이션

학번: 2010-20294

감사의 글

먼저 지도교수이신 정연준 교수님께 감사를 드립니다. 몸이 아파 연구활동을 거의 못할 때도 있었는데 걱정 말라고 말씀해주시고 또 기다려 주신 덕분에 무사히 박사과정을 마칠 수 있었습니다. 포닥으로 우리 연구실을 방문하셨던 심영선 박사님께도 감사합니다. 교수님께서 안식년으로 안계신 동안 그룹미팅을 주관해주시고, 특히 제 연구 및 논문 집필을 지도해주신 제 2의 스승님이 되 주셨습니다. 대학원 수업을 통해 많은 것들을 가르쳐 주신 이상엽 교수님, 신석민 교수님, 석차옥 교수님께도 감사드립니다. 또 논문 심사를 위해 멀리서 자리해 주신 성봉준 교수님께도 감사합니다. 연구실 1기 멤버들인 상원이형, 은상이형, 대건이형, 소리형도 고맙습니다. 형들이 만들어둔 협조적이고 건강한 분위기에서 맘편히 연구활동에 매진할 수 있었습니다. 저와 같이 연구실 2기 멤버인 인록, 현태, 찬우에게도 고마움을 전합니다. 기탄없이 이야기할 수 있는 동기들이 있어 대학원 생활이 한층 순탄했습니다. 연구실에 새로 들어와 굿은 일을 도맡아 하고있는 계현과 재학도 고맙습니다. 마지막으로 과학자라는 모호했던 제 꿈을 말없이 지지해준 가족들에게 고맙다는 말을 하고 싶습니다. 혼자 힘으로 해낼 수 있는 직업이라고 생각해서 과학자가 되었는데 돌이켜 생각해보니 많은 분들께 도움을 받았습니다. 그 모든 분들께 제가 받은 것과 같은 행운이 함께하길 바래 봅니다.